The thermo-electrochemical flow cell

Design, optimisation, & assessment

C. IJ. Reichert

Technische Universiteit Delft

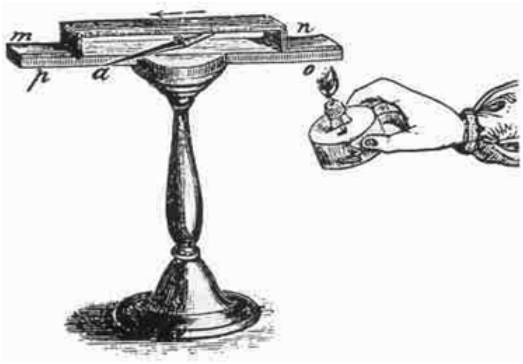

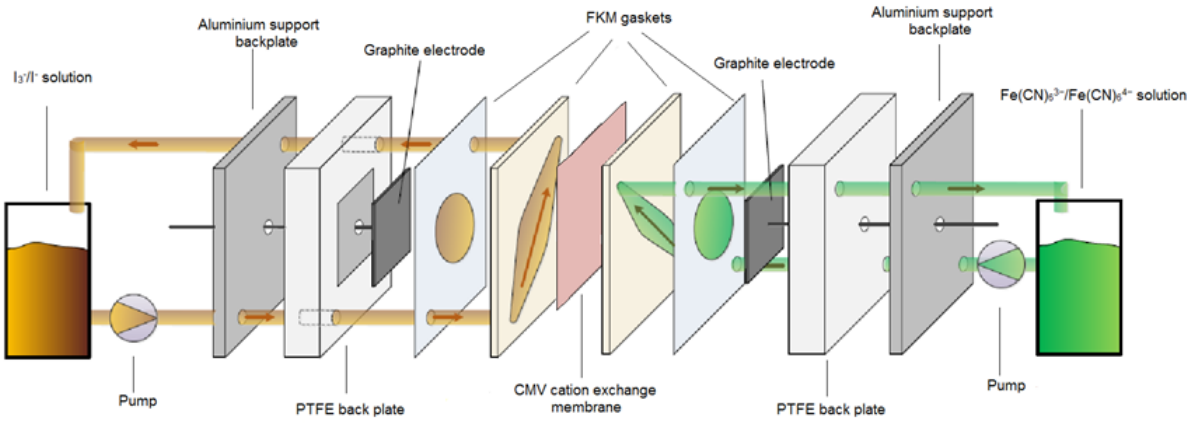

TU Delft Delft University of Technology

Challenge the future

The thermo-electrochemical flow cell

Design, optimisation, & assessment

by

C. IJ. Reichert

in partial fulfillment of the requirements for the degree of Master of Science in Chemical Engineering
at the Delft University of Technology,
to be defended publicly on Friday July 6, 2018 at 14:00 .

Student number:	4302265	
Project duration:	September 4, 2017 – July 6, 2018	
Thesis committee:	Dr. ir. D. A. Vermaas,	TU Delft, supervisor
	Prof. dr. ir. C. R. Kleijn ,	TU Delft
	Dr. P. E. Boukany,	TU Delft

This thesis is confidential and cannot be made public until December 31, 2018.

An electronic version of this thesis is available at `http://repository.tudelft.nl/`.

TU Delft

Abstract

In a world with ever increasing power consumption, it is important to use energy efficiently and responsibly. Currently almost 2/3 of chemical energy is wasted in the form of low grade waste heat (<150°C). This heat can be converted to electricity within the thermodynamic limit using thermoelectric materials. In the current work a thermo-electrochemical flow cell has been designed and improved. This novel design physically separates the hot and cold electrode by using two redox flow cells thereby creating a largest possible continuous temperature difference with electrolytes flowing between the cells. It also combines 2 different electrolytes in an attempt to get a high Seebeck coefficient. From measured and extrapolated values the current system could achieve a Seebeck coefficient of -2.88 mV K^{-1} and a temperature normalized power density of 2.40 $mWm^{-2}K^{-2}$. Currently no higher values than either have been reported for aqueous electrolytes and therefore a small breakthrough has been established in this work. In practice the values were somewhat lower at -2.02 mV K^{-1} and 0.33 $mWm^{-2}K^{-2}$ respectively. Unfortunately the current system is not very efficient and only managed to get a relative efficiency versus Carnot of 0.03%. Even though the performance of the presented system did not reach the expectations, it shows real promise and with slight alterations could be a viable candidate for utilizing low-grade waste heat.

Furthermore the degradation and decrease in concentration of the electrolytes were monitored. To analyze these changes titration methods were developed along with an absorption model. These methods were implemented with some success and require further development to be used accurately.

C. IJ. Reichert
Delft, June 2018

Acknowledgements

This page is dedicated to all the people who helped me through this project. Without their help and input I would have not gotten as far as I have. I has been a long journey with varying results but in the end I believe the results are intersting and invite further investigation.

The first person I would like to thank is my supervisor David Vermaas for letting me do this project and guiding me through all the steps to get it to where I am. Without his help and thoughts the entire project would have looked very different and would likely have never gotten the results it has gotten.

I also appreciate that the committee members, Chris Kleijn and Pouyan Boukany, have given me the opportunity to defend my thesis and thereby allowing me to be able to get one step closer to finishing my master's degree.

Next I would like to thank all the technical staff Christaan, Evert, Stefan, and Duco. They helped me with all the practical aspects, especially with regards to ensuring that the setup does not leak and thinking of designs that were resistant to the used electrolytes. They also wrote the programs that could read the thermocouple data for which I am very grateful. Additionally they helped with a few design challenges in particular with the heat exchanger.

The concentration analysis would not have been possible without the help of Baukje Terpstra and Ruben Abellon. Baukje did all the ICP-MS measurements which allowed me to confirm changes in the concentration and the cause of these changes. Ruben allowed me to use the UV-VIS equipment along with teaching me how to use it and without him the concentration measurements would have become very difficult.

Finally I would like to show some appreciation for all the members of the TP group who helped me get through my thesis. Without them it would have been a boring and long project but the time has flown by seeing as I started 9 months ago and it has only felt like a few months. The various students in the lab also helped me pass the time during the long days of measurements.

Nomenclature

Roman symbols

ΔG	Gibbs energy	J
ΔH	Enthalpy	J
ΔS	Change in entropy	J/K
A	Surface area	m^2
C	Concentration	mol/m^3
C_p	Heat capacity	J/K
D	Diffusion coefficient	m^2/s
E	Potential	V
F	Faraday constant	$96485\,C/mol$
i	Current	A
l	Length	m
n	Number of electrons in half reaction	mol
P	Power	J/s
Q	Energy	J
Q	Volumetric flow rate	m^3/s
R	Gas constant	$8.314 Jmol^{-1}K^{-1}$
R	Resistance	Ohm
r	Radius	m
T	Temperature	K
U	Potential	V
u	Mobility	$m^2 s^{-1} V^{-1}$
W	Work	J
z	Charge	–
ZT	Figure of merit	–

Greek symbols

α	Seebeck coefficient	V/K
δ	Diffusion boundary layer	m
η	Efficiency	–
η	Overpotential	V

κ	Electrical conductivity	S/m
λ	Thermal conductivity	$W/(m*K)$
μ	Dynamic viscosity	$Pa*s$
σ	Electrical conductivity	S/m
θ	Temperature coefficient	K^{-1}

Abbreviations

FKM	Fluoroelastomer containing vinylidene fluoride and other monomers
HE	Heat exchanger
$ICP-MS$	Inductively coupled plasma mass spectrometry
OCV	Open cell voltage
ORC	Organic Rankine cycle
PP	Polypropylene
$PTFE$	Polytetrafluoroethylene
$UV-VIS$	Ultraviolet-visible
XPS	X-ray photospectroscopy

Contents

1

Introduction

In a world with an ever increasing power consumption and an intensified focus on carbon emissions it is important to produce and use power as efficiently as possible. Currently most power plants waste up to 2/3 of all chemical energy available,[1,2,3] mainly in the form of low-grade waste heat and various other industries waste similar percentages of energy. The total production of waste heat in the United States alone is estimated at about $1.28*10^{15}$ kJ per year[4,5] (equivalent to approximately 9% of the US electricity production in 2017[6]) all in a temperature range of 25-150°C which shows there are huge gains to be made even if only a small percentage of this heat is converted. At these temperatures it is difficult to maintain steam that can be used for heating other processes. Therefore, it is often discarded which along with carrying an environmental burden also has a financial burden. On the other hand many processes require rigorous cooling which is most often done with cooling water which is subsequently discarded. A prime example is data centers which require large amounts of cooling which produces heated liquids that are then often left unused.

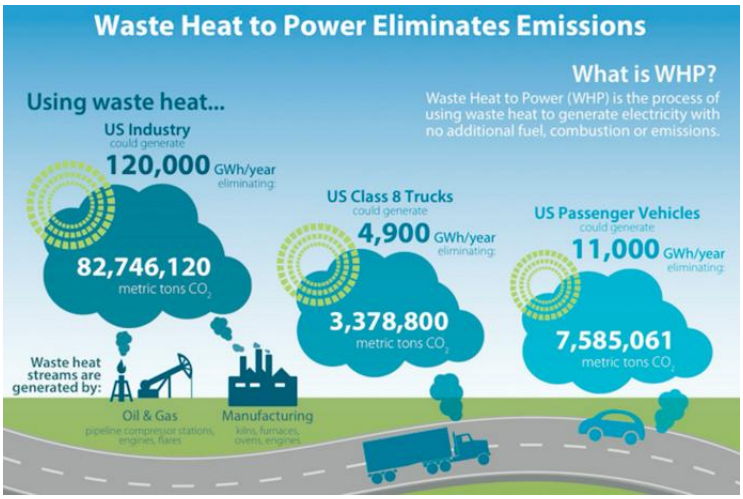

Figure 1.1: An info-graphic showing the potential waste heat utilization has to produce power and decrease emissions.[7]

Due to the large amount of energy available, a variety of techniques have been established to use as much of this waste heat as possible. Unfortunately, it has proven difficult to maintain efficient conversions due to thermodynamics limiting the maximal efficiency. The 2nd law of thermodynamics makes it difficult to convert heat efficiently and this conversion has been enshrined in the Carnot equation for heat engines. This equation can be found in section 2.2 and assuming we can use the full temperature range (0-100°C) of liquid water at atmospheric pressure, a maximum thermal-to-electrical energy conversion efficiency of 26.8% can be obtained. Additionally, the low temperatures associated with low-grade heat result in a small thermal

gradient which means it will often take tremendous amounts of surface area or time to be able to transfer all the heat available which will strain the economic viability. This means that the methods for harvesting waste energy become more and more complicated as the temperature decreases. In particular once the threshold of 100°C is crossed it becomes increasingly difficult as vapor-liquid systems become less usable.

A currently commercially exploited heat-to-power method is the organic Rankine cycle (ORC).[8,9] This method works by vaporizing and condensing organic compounds in a particular temperature range. These compounds have different boilings points than water which allows them to function within the 0-100°C temperature range. While possible to work below 100°C, these systems work better a higher temperatures which reduces their usability. Another downside is that this method produces mechanical work which then needs to be converted to electricity and this conversion will result in another efficiency loss in the system. There are a few other cycles like the ORC which use a varying composition of the working fluid to attain high efficiencies(>30%) however the downsides of the ORC are applicable to these systems as well.[10]

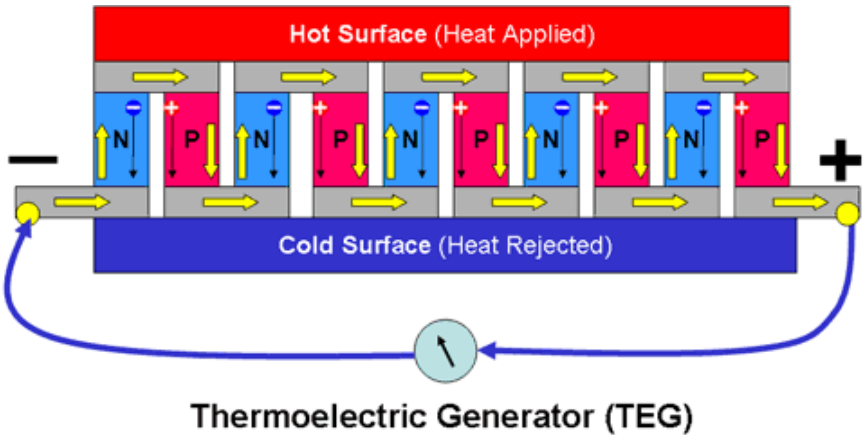

Figure 1.2: An example of a generic thermoelectric generator. One side of the material is heated and the other cooled with thermoelectric elements in between. This example contains both p- and n-type elements with opposite Seebeck coefficients allowing them to be added and therefore they are connected in series. The most used solid thermoelectric materials are metal tellurides.[11]

Another method which converts heat into electricity directly is thermoelectrics. This phenomenon was discovered in the early 1800s when it was discovered that when certain solids are heated on only one side, an electric current formed within them.[12] This discovery led to the creation of thermoelectric generators, which were made of various metals and salts and often operate in very large temperature ranges.[13] The driving force for the electricity production is called the thermoelectric effect which is characterized by the Seebeck coefficient. The determination and derivation of the coefficient will be explained in section 2.2.1. Some examples of thermoelectrics being used in practice are spacecraft,[14] deep-sea generators,[15] and off-grid power generation.[16,17] Thermoelectric generators are particularly effective for these applications as they usually have a limited size to power production ratio compared to conventional steam based engines along with the fact that they are easy to install and often do not have moving parts, which reduces maintenance needs. Unfortunately, the Seebeck coefficient is relatively low in solid state materials[18] which means that they have limited applicability in low-grade waste heat conversion as well as having heat transport issues.

This realization led to the discovery of liquid based thermoelectrics. This technique works with redox couples which circulate between two electrodes at different temperatures. This specific design has been called a thermogalvanic or thermo-electrochemical cell. This field progressed rapidly and the most commonly used redox couple is $Fe(CN)_6^{3-}/Fe(CN)_6^{4-}$ which has a high Seebeck coefficient along with a variety of other advantages(stability, current density etc).[18,19] This led to the standard design of a planar thermocell with heated electrodes and a static electrolyte. This standard design has been altered and optimized very often in an attempt to achieve commercial viability. The current work is somewhat different from this design but still

operates on the same theoretical basis.

These optimizations can be divided into three general categories. These categories are optimizations in the thermal gradient, electrolyte composition and redox kinetics. To improve the kinetics, extensive research has been done into the design of the electrodes used in the thermocell. The main method is by nanostructuring the carbon-based electrodes which can be done by adding multi-walled or single-walled carbon nanotubes.[20,21,22,23,24] These methods primarily increase the specific surface area allowing for faster kinetics. Another method is functionalizing the electrodes by means of doping to change their electrical properties rather than the surface area.[25] The electrolyte composition can be varied quite strongly with the goal of trying to achieve an as high as possible Seebeck coefficient. This coefficient can be increased by changing the active redox compounds(e.g. ionic liquids),[26,27,28,29] by introducing additives[30] which can stabilize redox species or by adding solvents[19] which will change the system entropy and thus increase the Seebeck coefficient. Finally, the thermal gradient can be optimized by physically separating the electrodes as done by Kazim et al.[31] or by placing a thermal separator in the cell which will keep the thermal gradient high.[32] The thermal gradient can also influence the mass transport to an electrode depending on the orientation of the cell.[18]

For the original design a variety of these factors was taken into account by physically separating the hot and cold cell and using a flowing electrolyte between the cells. The objective of this thesis is to improve and optimize this cell setup designed by Jorrit Bleeker.[33] This optimization will take into account the factors described in the previous section and will look at creating a continuous flow system which has a high versatility in design and use. Additionally, an important part of this thesis will be to evaluate and validate theoretical work previously done by Jorrit Bleeker. The main goal of this work is to assess the performance and efficiency of the designed flow cell. Further research goals can be found in section 2.5. This thesis will draw design inspiration from previously done work on redox flow batteries and more exotic thermocells.

This thesis will be structured as follows. Chapter 1 is the introduction. In chapter 2 the theory behind electrochemical cells will be explained and the research goals and questions will be formulated. Chapter 3 will detail the setup and the methods with which all the data was gathered. Chapter 4,5 and 6 contain all the results as well as the resulting discussion and evaluation. In the final 2 chapters the conclusion and recommendations for future work and applications of the used thermo-electrochemical setup are presented.

2

Theory

This chapter will describe the theory behind the presented research. It will describe previously established designs the current research is based on and how the viability and efficiency of the designed system is determined.

2.1. Electrochemistry

The key parameter in this thesis is the electrochemical reaction occurring at the electrodes. This reaction is defined as a redox(**red**uction-**ox**idation) reaction and takes the following form,

$$A^m + ne^- \rightleftharpoons B^{m-n} \tag{2.1}$$

where the compound of one half-cell gains or loses electrons and in the other half-cell the opposite happens. This half-reaction requires a certain potential(half reaction(cell) potential) which can be determined by cyclic voltammetry. Using the half cell potential, the full cell potential can be determined which in turn can be used to calculate the Gibbs energy using equation 2.2.

$$\Delta G = -nfE_{Cell} \tag{2.2}$$

Here ΔG is the Gibbs energy, n is the amount of electrons, f is the Farday constant and E is the cell potential. This equation will be used to determine the Seebeck coefficient which will be explained in greater detail in section 2.2.1. Equation 2.2 also determines the spontaneity of a given redox cell which also explains why batteries discharge once the circuit is connected. The half-cell potentials for the used redox couples($Fe(CN)_6^{3-}/Fe(CN)_6^{4-}$ and I_3^-/I^-) have been determined to be +0.44V and +0.66V respectively by Jorrit.[33] This results in a full cell equilibrium potential of +/-0.22V depending on how the cell is connected. The heated cell will determine at which applied potential the cell will be charged. The equilibrium potential values also imply that when the electrolytes mix only two compounds will remain (in this case iodide and ferricyanide).

2.2. Thermo-electrochemical cell

The viability of a thermo-electrochemical cell is dependant on many parameters. The main driving force for thermoelectrics is the Seebeck effect while the main loss is a result of the resistance. In the following sections both these parameters and their influence on the current work will be elaborated.

2.2.1. Thermo-electric effect

The thermo-electric effect causes p- and n-type behavior in thermoelectric materials similar to semiconductors. The thermo-electric effect encompasses three different effects: the Seebeck, Peltier, and Thomson effects. For this research only the Seebeck effect is of interest as it describes the phenomenon that when a surface is heated the active charge carriers(holes or electrons) will move towards the cold or the hot surface. To quantify these effects they have been given a value called the Seebeck coefficient. Depending on which

charge carrier is dominant, this coefficient is positive or negative for a certain material. The unit of the Seebeck coefficient was determined to be V K^{-1}. This unit can be explained by doing a derivation using the Gibbs energy.

$$\alpha = \left(\frac{dE}{dT}\right) = \frac{\Delta S}{nF} \tag{2.3}$$

Equation 2.3 shows the result of derivation. The entire derivation can be found in Appendix A. As can be seen the Seebeck coefficient in dependent on the change of potential with temperature which is itself dependent on the change in entropy of a given reaction. This means that the theoretical Seebeck coefficient can be calculated using the entropies of various redox species. However this is very difficult as not much literature detailing the entropies of electrolytes is available. Therefore, the Seebeck coefficient is often obtained experimentally by determining the open cell potential(OCV) at various temperatures and then plotting these values to obtain the coefficient.

The first applications originated from the semiconductor industry as most semiconductors have a Seebeck coefficient in the order of μV K^{-1}.[18] Such a low coefficient means that a large temperature difference is required to produce any significant amount of electricity. However the required high temperatures can be used for heating steam in industry whereas low temperatures are abundant and cannot be used for this application. Therefore a different class of thermoelectric materials have to be used. This led to the conception of liquid thermoelectric materials which had an associated Seebeck coefficient was of the order of mV K^{-1}.[34,35] This meant that these materials could operate in a much smaller temperature window and could be used to convert low-grade heat into electricity. Using this electrolyte resulted in a cell design very similar to a normal electrochemical cell with the main difference being that one of the electrodes is heated and the other electrode is cooled. Therefore many types of redox couples have been tested to find the couple with the highest coefficient. Currently, for aqueous solutions, the archetypical redox couple is the $Fe(CN)_6^{3-}/Fe(CN)_6^{4-}$ couple with a coefficient of approximately -1.4 mVK^{-1}.[18,19]

Once this couple was established a multitude of techniques was developed to enhance the coefficient for a particular redox couple. Research by Kim et al.[19] showed that adding solvents to the electrolyte can increase the coefficient to almost double the original solely aqueous value. Another method is passivization of certain ions so that they cannot spontaneously dissociate.[30] This allows for a higher stability of the ionic species and therefore a higher conversion. There are other methods which can also increase this coefficient drastically, however they change the entire nature of the system. They work by using an ionic liquid, but this method would not be suitable for the design of the current work as ionic liquids have a very high viscosity which would require much more energy to pump the liquid around which would likely negate any potential gains. On the other hand these ionic liquids have shown Seebeck coefficients up to 2.19 mV K^{-1}[18] and can operate in a much larger temperature range than aqueous solutions.

2.2.2. Losses in a thermo-electrochemical cell

While the Seebeck coefficient is the driving force, there are many sources for electrical losses. The main source of these losses is an applied overpotential. The overpotentials that affect the power output are the ohmic, the mass transfer, and the charge transfer overpotential. This overpotential translates to a resistance when it is divided by the applied current. All these resistances can be added to get the total resistance as can be seen in equation 2.4.

$$R_{Total} = R_{Ohmic} + \underbrace{R_{Mass} + R_{Kinetic}}_{\text{Non-Ohmic}} \tag{2.4}$$

The ohmic overpotential can be decreased by a variety of factors. Important for this ohmic overpotential or corresponding ohmic resistance is the design of the cell. A particularly large decrease is seen when the inter-electrode distance is decreased. This is a result of the way resistance is defined even though this definition is not entirely accurate for liquids (see equation 2.10). Another method for decreasing the ohmic resistance is by increasing the conductivity of the solution. This can be done by adding more charge carriers(in the current work potassium ions) by means of increasing the salt concentration. While not true for all electrolyte concentrations, the definition of conductivity implies that at a higher salt concentration a liquid becomes more conductive. Increasing the temperature can also influence the ohmic resistance. At higher temperatures the mobility of the ions is higher so they can more easily conduct charge and therefore decrease resistance.

The mass transfer overpotential can be decreased by increasing the rates of diffusion, convection, and migration. These parameters have a large influence in stationary electrolytes as at some point a large boundary layer could form. A method to decrease this mass transfer resistance is by increasing the concentration of the working electrolyte. This causes a higher concentration gradient which in turn increases the amount of diffusion. Another method is by increasing the flow rate along the electrode. This flow will dissipate a portion of the boundary layer by providing "fresh" ions thus keeping the concentration difference higher. It effectively prevents concentration polarization and therefore decreases resistance. This method influences both the convective and diffusive properties of the liquid. The true defining parameter for the flow is the residence time as if the contact surface area was increased without changing the flowrate, polarization will occur due to a build up of oxidized/reduced species. Increasing the temperature is an approach that also impacts the mass transfer. It affects the mass transfer by increasing the mobility of ions. In conventional thermo-electric cells this temperature is also used as a gradient between the electrodes which allows for both thermal diffusion and convection between the electrodes. Thermal diffusion is caused by heated particles moving near the heated surface and depending on the orientation of cell convection moves the heated liquid towards the cold electrode and vice versa.

The charge transfer overpotential depends on the kinetics of the redox reaction at the electrodes. To decrease this overpotential a lot of research has been done to functionalize the electrodes. A crude method is by increasing the surface area by using a larger electrode but a more sophisticated methods include: using multi-walled carbon nanotubes(MWNT) to increase the specific surface area,[20,23] by doping the electrode to improve the already present p- and n-type characteristics,[25,36] or by changing the electrode material. This is interesting for the current work as it has been shown that graphite can outperform even platinum as an electrode.[37] Figure 2.2.2 gives a schematic overview of a conventional thermo-electrochemical cell. As can be seen the ions move between a heated and a cooled electrode thereby converting thermal into electrical energy.

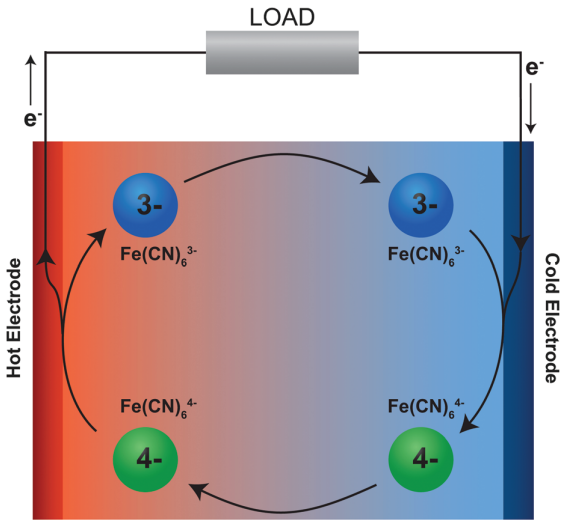

Figure 2.1: An overview of a generic thermocell with the associated reactions. This cell details the reaction occurring with the $Fe(CN)_6^{3-}/Fe(CN)_6^{4-}$ redox couple. From Dupont et al.[18]

To be able to compare the performance of thermo-electric devices, a figure of merit was established. The equation describing this figure of merit is presented below where α is the Seebeck coefficient, σ is the electrical conductivity, and λ is the thermal conductivity.

$$ZT = \alpha^2 * \frac{\sigma}{\lambda} \tag{2.5}$$

This equation was designed to be used for solid state thermo-electric devices and this was recognized by Dupont et al.[18] so they modified it to be used for a thermocell using an electrolyte. Unfortunately their altered equation will also not be applicable to the design of the present work and therefore the efficiency relative to the Carnot efficiency and the temperature normalized power output will be used as an overall indicator of performance. Equation 2.6 describes the Carnot efficiency and shows that it is dependent on the difference

between the high and low temperatures which for the current work is not very high thus resulting in relatively low efficiencies. For example using the temperatures at the extremes of the proposed operational range(293K and 353K respectively) a maximum heat-to-work efficiency of 17% can be obtained.

$$\eta_{Carnot} = 1 - \frac{T_C}{T_H} \tag{2.6}$$

2.2.3. Literature inspirations

The current work deviates strongly from the previously mentioned standard thermo-electrochemical setup. Therefore inspiration was drawn from other works that have made an exploratory attempt into similar systems. In the following paragraphs are a few examples of other systems and how they differ from the current works design.

The idea for an thermo-electrochemical cell with a moving electrolyte is not new. The earliest known recorded system with a moving electrolyte was described in 1886[38] but it does not give any further information other than the design. The earliest modern liquid flow system for heat to power was explored by Hammond et al.[35] with the largest difference being that they used salts with a poor stability as well very unselective membranes which resulted in a system with a poor performance. However, they laid the groundwork as to what requirements a flow cell must meet to be able to function efficiently and they made calculations where they could reach up to 50% of the Carnot efficiency. Unfortunately due to the many drawbacks of the system in a novel setting, it received little attention and was therefore never explored further. Even with all these drawbacks, the current design is similar and the research by Hammond et al.[35] serves as a strong theoretical basis for the current work.

Kazim et al.[31] designed a flow system using a single electrolyte(the $Fe(CN)_6^{3-}/Fe(CN)_6^{4-}$ couple) . Its design basis is similar to the current system as both physically separate the electrodes and use heat exchangers to maintain a large temperature difference. Additionally, their design is aimed at reusing low grade waste heat, however their testing of the system was limited as they only measured the OCV and short circuit current thus not getting true output values for their design. The current system differs by using two electrolytes as well as getting more extensive efficiency data. It also uses two cells and can accommodate a wider range of heat sources.

Lee et al.[39] are another design influence as they used two different redox species to increase the Seebeck coefficient. The main difference with the current system is that they used solid state electrodes with only a supporting electrolyte. This mean that the electrodes had to be physically moved or cycled to allow for heating/cooling. They did report a combined Seebeck coefficient of -1.2 mVK^{-1} which unfortunately is lower than using just the $Fe(CN)_6^{3-}/Fe(CN)_6^{4-}$ couple as an electrolyte. However even with this low coefficient they managed to achieve a heat-to-power cycling efficiency of 3.7% without attempting any heat recuperation(5.7% with 50% recuperation). This relatively high efficiency means that this setup shows great promise and with some alterations could be economically viable. Their method also showed great cycling stability with only a minimal loss in efficiency over 40 heating and cooling cycles.

2.3. Redox flow battery

Redox flow batteries form the second part of the design basis for this project. Redox flow batteries have been developed for multiple purposes. Their main purpose is to function as grid levelers as they will charge when surplus electricity is produced and will discharge when not enough is produced.[40] In the meantime the electrolyte is stored in a tank which gives them their battery characteristic as they build up stored energy in these tanks. They function by letting electrolytes flow past electrodes where they can undergo a reversible redox reaction. Of all the electrolyte systems, the all-vanadium cell is the most developed and it has already been implemented on a large scale.[41] This cell involves using vanadium ions at various states of charge in an acidic solution. Using these materials also introduces the downside of this design as it has a high toxicity and is quite expensive.

There are various factors which determine the efficiency and viability of a redox flow battery system. Firstly there is the energy density as this will influence the size of the system and the required amounts of electrolytes. This density is often defined as W/L or W/kg of solution. Related to this energy density is the state of charge which shows how much ions have been reduced or oxidized of the total amount as at some point the system will experience increased resistance to the conversion due to low concentrations of the active ionic species.[43]

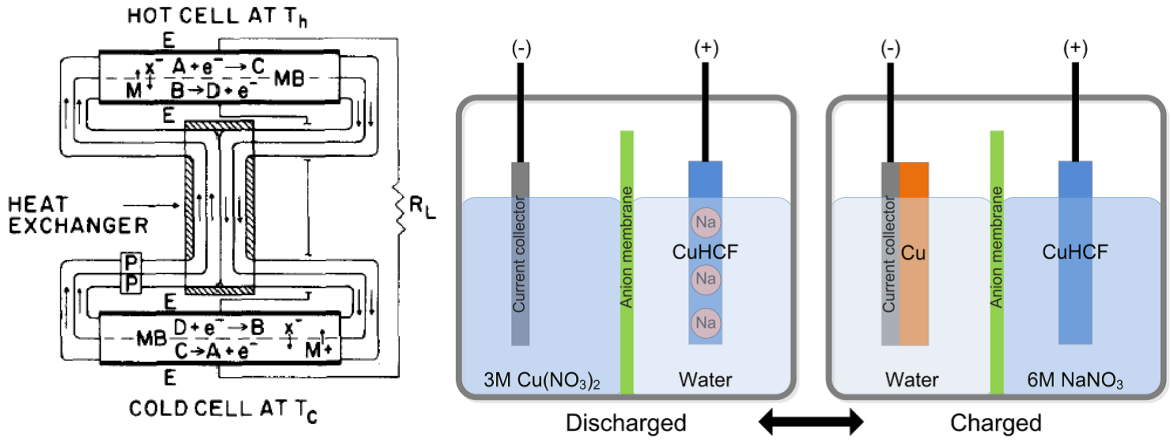

(a) (b)

Figure 2.2: (a) The cell design used by Hammond et al.[35] as can be seen they used a setup with 2 cells and a heat exchanger in between with charging happening in one cell and discharging in the other. (b) The setup designed by Lee et al.[39] They charged and discharged a small cell which then would be moved to allow for heating and cooling. As can be seen they are dependent on the deposition of copper and sodium depending on which part of the power cycle they are in.

Aside from these factors there are also major restrictions on which type of electrolyte can be used. Firstly the electrolytes for both half cells need to be stable at the same conditions(pH, temperature, pressure). Next they need to be separable by a membrane as high crossover of ionic species will drastically reduce the efficiency of the cell and cause possible side reactions. High ionic crossover is detrimental to the long term operation and will therefore be investigated in the current work as well. Finally, the half cell potential of each species should be within the oxygen and hydrogen evolution reaction potentials as otherwise those half reactions will occur instead of the desired half reactions.[43]

The current report uses various aspects of the redox flow battery. The main design parameter that has been incorporated, is the flow characteristic which will allows us to move the electrolyte from the hot cell to the cold cell and will improve mass transport by having a non-static electrolyte. Secondly similar restrictions are valid for the electrolytes in our setup and therefore a half cell couples have been chosen that adhere to all the design parameters. As mentioned in section 2.1 these couples are $Fe(CN)_6^{3-}/Fe(CN)_6^{4-}$ and I_3^-/I^-. Lastly the factors that govern the viability of a redox flow battery can also be used for our setup as parameters like energy density and the state of charge are relevant for this research.

2.4. Thermo-electrochemical flow cell

As previously stated the design of the cell in this thesis is a combination of the above techniques. This combination resulted in a setup with two cells that are connected by tubing and a pump. This allows for the incorporation of heat exchangers which creates the opportunity for a large temperature difference. A further visual elaboration of this design can be found in Appendix C. The half cells of each cell contain different compounds. Using two compounds with different Seebeck coefficients has been reported by Lee et al.[39] with the main difference with our cell being that they used a solid state medium to hold the charge and had a static electrolyte. This means that cooling and heating processes take significantly more time as well as requiring manual movement of the cells. Using two different compounds changes the overall Seebeck coefficient of a cell. It was found that the full cell Seebeck coefficient can be calculated using a formula analogous to the formula used for the calculation of a cell potential. This formula can be seen in equation 2.7.

$$\alpha_{Full} = \alpha_{Red} - \alpha_{Ox} \tag{2.7}$$

The value of this full cell Seebeck coefficient determines whether power can be obtained from the hot or cold cell. If the value is negative the electrolyte needs to be charged in the hot cell and discharged in the cold cell as $\Delta E_{Hot} < \Delta E_{Cold}$. The opposite is required when the value of the Seebeck coefficient is positive. This is visually represented in figure 2.4 which shows that the difference between these energy levels is the work that can be taken out of the system.

Using this cell coefficient the efficiency can be calculated by taking the energy out and dividing it by all

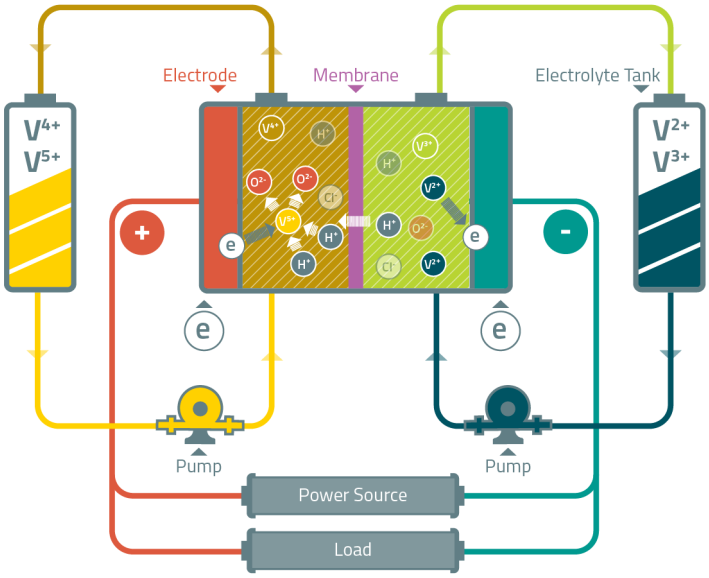

Figure 2.3: A schematic of how the all vanadium redox flow battery functions. The electrolyte can be stored in the the tanks and unloaded when there is a shortage of grid electricity. From Australian Vanadium[42]

the energy that has been put into the system. For the system described here this will result in equation 2.8. The derivation for this equation can be found in appendix A.

$$\eta_{full} = \frac{W_{out}}{Q_{HX} + Q_{Pump}} = \frac{\alpha \Delta T I - (R_{Charge} + R_{Discharge}) I^2}{\dot{m} * C_p \Delta T + \Delta P_{Total} * 2Q} \tag{2.8}$$

This equation will give the value for the absolute efficiency of the system but the efficiency relative to the Carnot efficiency is also of interest as it would give a better indication of how much of the available energy is converted. Equation 2.8 shows that to maximize the efficiency the Seebeck coefficient, heat exchanger efficiency, and the temperature difference between the cells need to be as large as possible whereas the resistance and pumping power and added heat need to be as low as possible. Figure 2.4 gives a visual representation of where the work of the system comes form and how charging at a higher temperature results in work being able to be extracted from the system instead of requiring it.

While equation 2.8 is often used to determine the viability of a system another important factor is the absolute output of power. It is important to know this value as when a very large setup only produces minute amounts of power the economical viability will drastically decrease. Equation 2.9 describes the maximum power output of the system.

$$P_{max} = \frac{(\alpha \Delta T)^2}{4(R_{Charge} + R_{Discharge})} \tag{2.9}$$

The value obtained from this equation will indicate if the power density of the system is viable. Unfortunately it only gives part of the picture by only taking the internal cell resistance as a loss it does not take thermal losses into account however it will be an indicator of the true potential of the designed system. A further derivation of the maximum power can found in Appendix A.

Another factor that determines the viability of a flow cell is the cycling stability. It has been well established that materials degrade over time and therefore it is important to know at what rate an electrolyte degrades. This degradation is not taken in to account with the previous equations as they will often be determined with a few cycles but for a cell to be economically viable it will need to remain operational for extended periods of time. The stability of liquid systems is often determined by which salts are used for the electrolyte. Due to impurities in the liquid or exposure to oxygen and sunlight many compounds degrade thereby decreasing the concentration of active species which will in turn reduce the cycling efficiency.

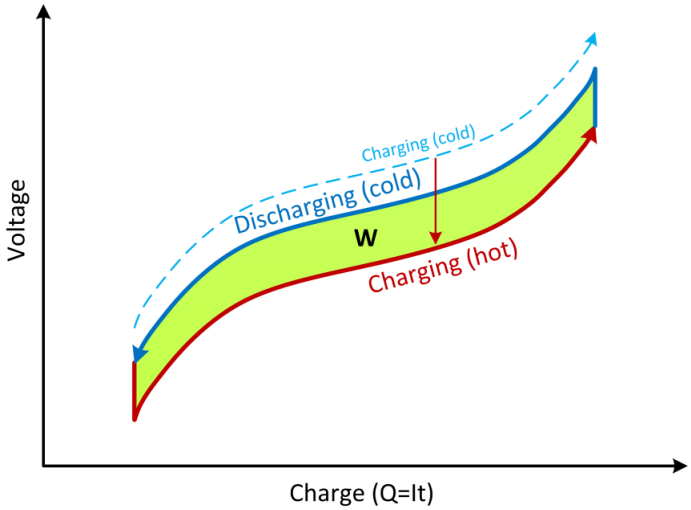

Figure 2.4: A schematic plot showing the voltage and charge. It shows how charging at a higher temperature allows for extractable work. Firstly, the cell is heated which lowers the cell potential. Next it is charged, where the potential increases during charging due to increased resistance. Then the cell is cooled which increases the cell potential en then during discharging an ideal cell follows the same line as during charging. The surface in between the charging and discharging cycle represents the extractable work. From Lee et al.[39]

The current design makes use of a flowing electrolyte. This flow has a few advantages compared to a static electrolyte with the main downside being the power requirement of a pump and therefore a loss of efficiency. The first advantage is that with this setup it is easier to create a difference in temperature as the electrolyte can be passed through a heat exchanger and therefore reuse heat instead of requiring extensive cooling to keep one side of the cell cooled. It also foregoes the use of a thermal separator as used by Hasan et al.[32] Such a separator increases the internal resistance and this design does not have that disadvantage. Using a liquid also allows for a better contact with the initial heat source as waste heat almost always come in liquid form and therefore common heat exchangers can be used to heat our solutions. Another more implicit advantage in the continuous supply of the redox species which results in a smaller boundary layer and thus a smaller internal resistance. Additionally, this also results in less mass diffusion resistance between electrodes as the electrolyte is forcibly pumped between them. Furthermore using two electrolytes allows for a much a higher Seebeck coefficient as explained with equation 2.7. This overcomes a problem often associated with thermoelectric cells as in general they have low Seebeck coefficients. By combining all the described factors the current design should have superior characteristics compared to conventional cells.

2.4.1. Resistance

From the above equations it can be seen that thermal and electrical efficiency are the key to creating a viable setup. The electrical efficiency is mostly determined by the internal cell resistance. As mentioned in section 2.2 there are various sources of resistance. For the current setup many of these sources are present and they can be manipulated. This manipulation will allow for lower resistance which will in turn improve the overall efficiency of the setup. Even though there are many sources of resistance, equation 2.10 encompasses most of these effects as almost all changes can be reduced to one of the parameters in this equation. In this equation l is the length through which charge is passed, A is the surface area through which the charge can pass, and the κ is the conductivity of the material.

$$R = \frac{l}{\kappa A} \tag{2.10}$$

Firstly, the electrolyte can be altered. This can be done at a very basic level by changing which compounds are used as they inherently have a particular Seebeck coefficient, stability, and solubility. For this work these electrolytes have already been chosen after extensive investigation into possible redox couple combinations by Jorrit Bleeker.[33] However it is still possible to make some adjustments particularly in the concentration of the electrolyte as when this increases the conductivity of the solution as well as concentration gradients increase which will overcome mass transport resistance as well as ohmic resistance. The concentration of the supporting electrolyte can also strongly influence the resistance. In the current work potassium cations are

used to carry/equalize the charge within the cell. Due to conductivity being a function of the concentration of all present ions, this supporting electrolyte can have a large influence. So the electrolyte can influence the conductivity in equation 2.10 as well as the α and C_p from equation 2.8.

Secondly, the resistance can be influenced by the cell design. As stated previously this can be achieved by increasing the electrode (specific) surface area. Another option is to change the electrode material. The material can change the kinetics of a reaction and therefore hinder or assist the conversion of active species and therefore limit efficiency. Another manipulable design choice is the inter-electrode distance. This distance will determine how far the charge needs to be carried and thus can have a significant impact on the resistance. Both these methods tie back to equation 2.10 as the electrodes change the A whereas the distance changes the l. Another cell design choice is the type of membrane that is used. While it is a cost consideration the design of the membrane can have a significant impact on the resistance it creates.[44] This can be seen in the research by Hammond et al.[35] in particular as they mention strong fouling of the membrane as the cause for increased internal resistance.

Finally, there are some more abstract parameters that can affect the resistance. As mentioned the flow rate can have an effect by decreasing the boundary layer. A second parameter are the temperatures between which the fluids are cycled. When the temperature is increased the mobility of ions increases which allows for charge to be transported quicker. Additionally, the active species move to the electrode surface quicker which reduces the ionic boundary layer and therefore reduces mass transport resistance. This behaviour is similar to a negative temperature coefficient thermistor. This effect results in a non-ohmic resistance as the resistance arising from it will not be proportional to the current.

2.5. Research goals & questions

The goal of this thesis is to make and test a working thermo-electrochemical flow cell. However only making the cell functional is only part of the goal. It will also need to be optimized in order to get a reasonable efficiency and power output for possible market applications.

- **What heat-to-power efficiency and absolute power output can be attained using a thermo-electrochemical flow cell?**
- How do the temperature difference, flow-rate, electrolyte concentration, and interelectrode distance influence the output parameters of the system?
- How stable is the power output over time?
- What are the drawbacks of the designed system?
- What is the extent of the crossover/concentration change over time?

3

Methodology

This chapter describes how the cell was designed and operated as well as how the electrolytes were prepared. It will also detail design decisions and how they optimize the system. Furthermore the procedure for doing the measurements and the analysis of the concentrations is explained.

3.1. Setup design

The cell design was based on a design previously used by David Vermaas.[45] The original design was scaled up to allow for larger scale experiments, in particular with a larger electrode surface area. The material selection was based on the resistance against the chemicals that were used in the experiment. This meant that most common metals and a large amount of plastics were not suitable due to the inevitable degradation after being in contact with the electrolytes. These restrictions led to the use of PTFE (polytetrafluoroethylene) for all major components that are in contact with the chemicals. Other components that were in contact with the chemical were made from polypropylene(PP) and other fluoro-elastomers. This led to the design used by Jorrit Bleeker.[33] However, it was discovered that silicone gaskets were not chemically compatible with the iodine solution which led to their degradation. Additionally, the cell suffered from leakages which hampered the operation and therefore the design had to be adapted.

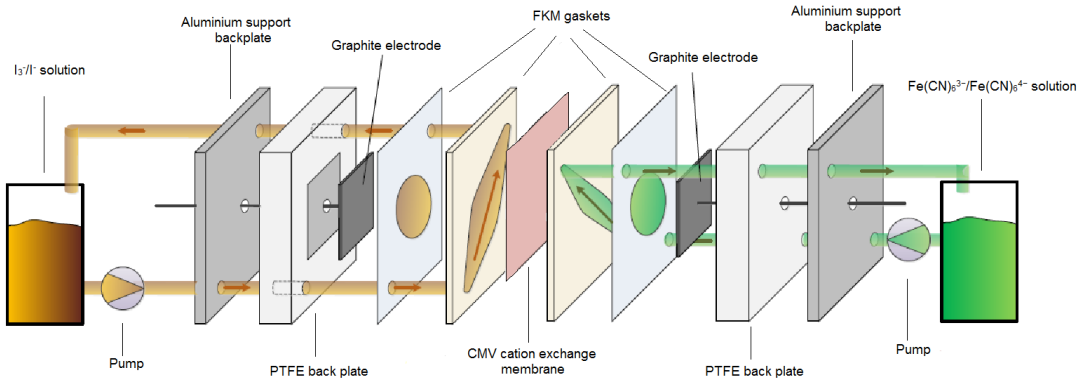

Figure 3.1: An exploded view of the cell used in the current work. The flow field within the gaskets at the membrane was filled with a PTFE mesh to give stability to the gasket. A cross-flow was used to limit contact time to only the inter-electrode area. While showing a direct flow to the beaker, in reality the electrolyte moves through multiple pieces of equipment. The electrolyte flows upward to minimize gaseous holdup in the cell which could hamper the flow of electrolyte. Adapted from Bleeker[33]

For this thesis, the design by Bleeker was slightly altered to improve performance. The silicone gaskets were replaced with FKM gaskets as they were both chemically inert and thin (400 μm). Additionally, extra holes were drilled into the corners of the cell to allow for more pressure at the in- and outlet of the electrolytes which would prevent leakage. The polyamide spacer used in his work was replaced by a PTFE mesh which

was embedded within a gasket which reduced the inter-electrode distance by 6.4 mm. The polyamide spacer warped at higher temperatures as well which made replacement necessary. This resulted in the cell seen in figure 3.1. The thermocouple design was also improved due to extensive damage occurring with the previous design. Over time the triiodide solution could leach through thin glue layers which resulted in corrosion of the thermocouple. The new thermocouple design can be seen in figure 3.2. Once the cell was finished, it was characterized with the techniques explained below. Following this characterization the entire setup was finished by incorporating two heat exchangers and adding the second cell to be able to assess the directly obtained power performance and efficiency of the setup. Technical data on all the components that were used for this research can be found in appendix B.

Over time not only the thermocouples suffered from damage due to the corrosivity of iodine and the reactivity of ferro/ferricyanide, but also the electrodes, wiring and the PP connectors suffered damage. The damage to the electrodes was particularly troublesome as it resulted in leakage and further damage to the wiring. Therefore a titanium electrode was tested the results of which can be found in section 6.2. Pictures of the damage that occurred can be found in appendix D.

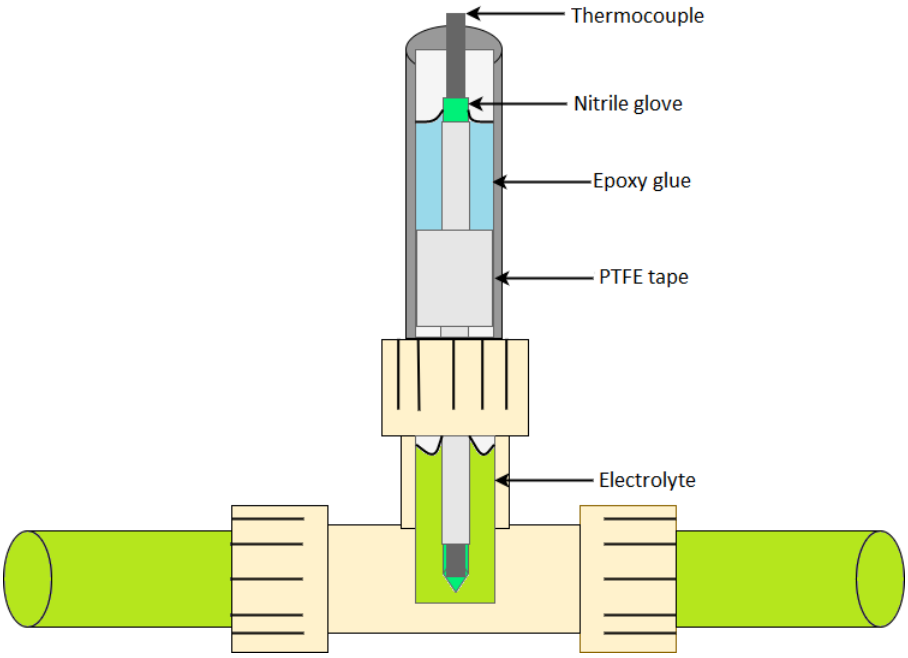

Figure 3.2: The design of the thermocouples. The thermocouple was placed inside a glove. This glove was wrapped in PTFE tape and stuffed into a PTFE tube to the extent that it is secured in place. Epoxy glue is then poured on top to make the entire design airtight as to prevent liquid from squeezing through.

3.1.1. Heat exchanger

After the cell was redesigned and improved, it was necessary to design a heat exchanger(HE) to improve the efficiency of the entire system as has been described in equation 2.8. This was quite a task as most conventional heat exchangers rely heavily on metals to conduct heat but, as previously stated, the electrolytes are not chemically compatible with most metals.

These restraints led to a final design which was based on a glass condenser that is used in many labs. Due to being made of glass, it satisfied the inert material criterion and could also provide sufficient heat exchange area and enough thermal conductivity to meet our requirements without being very large. This design can be seen in figure 3.3. It was custom made as it required some unique parts to be able to be incorporated in the setup. The final design had an internal surface area of nearly 0.5 m^2 which is quite large for its size. This was made possible by having an outer and an inner coil. The heat exchanger was operated in counter-current flow to maximize the heat exchanging capacity. Maximizing the heat exchange would improve overall efficiency of the design. The final calculations for the design of this heat exchanger can be found in appendix F. It is once again a somewhat versatile design and could be used for other applications that have similar restraints and requirements as the present work.

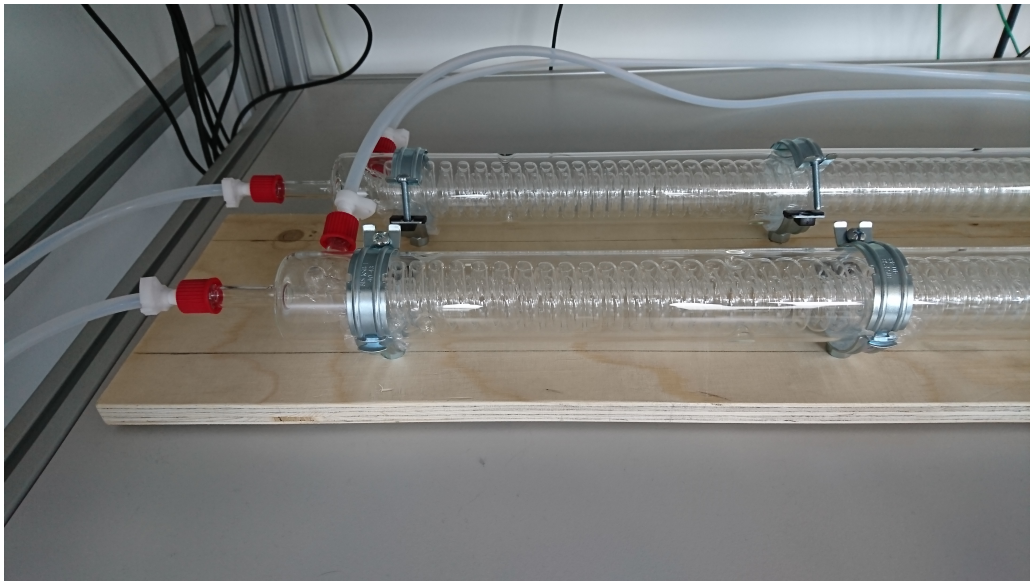

Figure 3.3: A picture of the end of the heat exchangers. As can be seen there are 2 coils inside the bigger tube. The outside tube volume was approximately 4 times bigger than the internal coil volume. The in- and outlets were attached so that the heat exchanger operated in counter-flow.

3.2. Cell operation

This section details how the cell was operated and how the measurements were performed. The setup was operated in two modes with the first mode using only one cell to be able to characterize the cell and the electrolytes and the second mode using two cells to get power output and efficiency data. When the temperature was increased, the next measurement was only started after the temperature had reached equilibrium. This was done in order to get a measurement without major temperature fluctuations. To measure the temperature, thermocouples were used. They measured the temperature at the inlets and outlets of the cell and were inserted directly into the electrolyte flow. Their values were averaged to get the approximate temperature at the electrodes.

3.2.1. Single cell characterization

Initial characterization of the cells was done using a single cell setup. A flow diagram with the various components can be seen in appendix C. It gives an schematic overview of what the system looks like and how all the equipment ties together to be able to perform the measurements. For initial OCV measurements the potential was measured when zero current flowed through the cell. This was done for multiple temperatures after which the results were plotted. For resistance and subsequent OCV measurements, a chronoamperometric method was used which applied a current starting at +90 mA followed by -90 mA. Following this method the current was cycled down to -10 mA with decrements of 10 mA. A plot of this method can be seen in section 4. The obtained data points were then imported to Matlab to calculate the area resistance(Ωcm^2). This method was used for all measurements on the influence of particular variables. Impedance measurements were performed by running the cell a at current until equilibrium was reached and then the impedance was measured between 500 and 50000 Hz, where the frequencies of interest are between 1000 and 10000 Hz. Appendix B gives an overview of the various equipment and components as well as the measurement programs that were used to perform these characterization measurements.

3.2.2. Two cell power generation

A process flow diagram for the characterization of the entire setup can be seen in appendix C. As can be seen the electrolyte is pumped around between both cells with cooling and heating operations in between. Furthermore the amount of thermocouples has been expanded, but they operate in the same way as for the single cell. To allow the setup to operate, the heat exchanger had to be filled with electrolyte before the entire setup was turned to remove as much air from the system as possible as otherwise the heat exchanger would not function. An electrical loop was made between the two cells and the potentiostat. A chronoamperometric

method was run at 12 currents with increments of 15 mA starting from the OCV. An example of this method can be seen in figure E.1. The output potential and current could then be multiplied to give the power output. Furthermore the efficiency was calculated using the equations in section 2.2 by calculating the pumping power and measuring the amount of heat added in the heating bath. For the stability measurement the cell was allowed to run for a long period of time at the maximum power output. Meanwhile the electrical power output was monitored to determine if the performance changed over this time period.

3.3. Electrolyte preparation

For the initial tests with a single cell, concentrations determined by Jorrit Bleeker[33] were used to verify his results. To make the solutions the molarities in table 3.1 were used. Both solutions were vigorously stirred in order for the salts to dissolve in an acceptable amount of time. The solubility and the dissolved amounts were calculated using OLI Studio which also provided data for constants that were used in various calculations. After initial testing the solutions were standardized to be able the assess different effects more accurately. This meant that the potassium ion concentration was set a 2 M. Using this guiding concentration the optimal concentrations for all electrolyte species were found and this optimized solution was used to test for all other variables in order to find the final optimal setup parameters. For the single cell characterizations solutions of 0.5 L were made while the setup had an internal volume of approximately 0.2-0.25 L. For the full setup a larger volume was required due to the large internal volume of the heat exchangers. 2 liters of solution was prepared but the actual internal volume of the setup was approximately 1.6 L.

It was observed that over time a red precipitate was formed in the ferro/ferricyanide flask. Using OLI studio it was determined this substance was most likely iron oxide which formed due to dissolved oxygen in the solution reacting with the iron atoms. Additionally, the colour of this flask changed to a darker green over time which would indicate a change in chemical composition. These changes will decrease the accuracy of the measurements due to a reduced concentration of the ferro/ferricyanide couple. This can also be seen in section 4.1 where the OCV shift for different measurements at the same conditions. The change in concentration was analyzed in chapter 6.

Table 3.1: Table containing the various chemicals and at which molarity composition they were tested during the initial testing and after standardization. The initial testing solutions were used to recreate Bleekers results and for the first experiments which tested the influence of the electrolyte concentration. However it was noticed that not all changes could be contributed to the active species and thus standardization had to be done. The test numbers are arbitrarily numbered and thus not necessarily performed in the presented order.

Initial testing

$Fe(CN)_6^{3-}$/$Fe(CN)_6^{4-}$ **solution (M)**				I_3^-/I^- **solution (M)**			
Chemical	**Test 1 (M)**	**Test 2 (M)**	**Test 3 (M)**	**Chemical**	**Test 1 (M)**	**Test 2 (M)**	**Test 3 (M)**
$K_3Fe(CN)_6$	0.1	0.05	0.3	I_2	0.1	0.05	0.3
$K_4Fe(CN)_6$	0.1	0.05	0.3	KI	0.3	0.15	0.9
KCl	0.3	0.35	0.3	KCl	0.7	2	0.33

Standardized solutions

$Fe(CN)_6^{3-}$/$Fe(CN)_6^{4-}$ **solution (M)**				I_3^-/I^- **solution (M)**			
Chemical	**Test 4 (M)**	**Test 5 (M)**	**Test 6 (M)**	**Chemical**	**Test 4 (M)**	**Test 5 (M)**	**Test 6 (M)**
$K_3Fe(CN)_6$	0.05	0.1	0.3	I_2	0.05	0.1	0.3
$K_4Fe(CN)_6$	0.05	0.1	0.3	KI	0.15	0.3	0.9
KCl	1.75	1.45	0.35	KCl	1.85	1.7	1.1

3.4. Concentration analysis

To determine the concentrations of the solutions, 3 analysis methods were used for both electrolyte solutions. One method to determine the concentration of one species and another method to determine the total concentration. The third method was to verify the accuracy of the other measurements. For the single species, titration methods were developed based on available information. While these titrations methods have been described, no manuals or previous data was available.

3.4.1. Iron(II) determination

For the titrations a stock of potassium permanganate solution was made by dissolving 3.161 g of $KMnO_4$ in 100 mL of demi-water to obtain a 0.2 M solution. For measurements this solution was diluted 200 times to a concentration of 1 mM which is the concentration assumed from here on when referring to the permanganate solution. The ferrocyanide sample was prepared by taking 1.5 mL of solution and slowly diluting this with 8.5 mL of 0.3 M sulfuric acid while vigorously stirring. This sample is then left in the fume hood for a minimum of 5 minutes to allow for the removal of the formed hydrogen cyanide. Then 1 mL of this acidic solution is taken out and diluted once more with 1 mL of 3 M sulfuric acid and 8 mL of demi-water. While this may result in an excessively low pH, it is done to ensure that all the iron ions are stripped of the cyanide ligands and the proper permanganate reaction occurs. Then the permanganate solution is slowly added to the solution until the final colour is reached.

The final colour is determined by adding known amounts of permanganate and ferrocyanide together. When this is done stoichiometrically it will result in a yellow/orange coloured solution. This colour occurs regardless of the presence of ferricyanide and potassium chloride being in the solution.

The total iron concentration was determined by ICP-MS (Inductively coupled plasma mass spectrometry, PerkinElmer Optima 5300). With this method the absolute iron and potassium content of the solution could be measured. By ionizing the atoms they lose their valence ratio but in combination with other measurements, the exact ratio can be determined. Using the values obtained for these measurements we could see if the actual iron content changed while monitoring the potassium content as well. A discrepancy between the two would show that there was a crossover and give an indication of how large it was.

To give further credibility to the accuracy of the concentration measurements, UV-VIS absorption measurements (Perkin-Elmer Lambda 40 UV-VIS photospectrometer) were performed. By diluting the samples 1000 times and scanning wavelengths from 250 to 650 nm relative concentrations could be obtained. Ferricyanide should exhibit an absorption peak at approximately 420 nm. Using this peak, the intensities could be compared due to the Law of Lambert-Beer. For determining the concentrations,a method was developed using reference absorption measurements at a fixed concentration. These references were then fitted to the actual measurements thereby producing the concentrations of the various species. Using matrix multiplication (A*x=b) where A are the reference samples, b is the measured sample, and x is the concentration vector, the concentrations could be determined.

XPS(X-ray photospectroscopy, Thermofisher K-Alpha XPS system) measurements were also performed on the electrodes that were in contact with this solution after discolouration of the electrodes was observed during measurements. The resultant spectrum was analyzed using a database of known spectrum values.

3.4.2. Triiodide determination

For the titrations of the iodide/triiodide solution ferrocyanide was chosen as a titrant due to the incompatibility of other titrants. For ease a ferrocyanide solution of 0.3 M was made. This solution was then diluted 5 times by taking 2 mL of this solution and adding 8 mL of demi-water. To prepare the iodine sample 1 mL of iodide/triiodide solution was diluted in 19 mL of demi-water. Then 4 mL of this solution is put in a separate beaker and ferrocyanide is slowly added to the solution until the required colour is reached.

The required colour can be determined in the same fashion as with the ferrocyanide titration. By titrating a known amount of triiodide with a known amount of ferrocyanide a light yellow colour (the colour of ferricyanide) is attained and this sample can be compared with the true titration and thus determine the appropriate end point.

The iodide/triiodide solutions were also investigated with UV-VIS absorption as the triiodide concentration could be investigated within the used wavelength range. The measurements were done using the same procedure as for the ferro/ferricyanide measurements.

The samples obtained here were also measured with ICP-MS. While this machine could not detect the iodine content it could detect iron and potassium. If any measurable quantity of iron would be present it would be a clear indication of crossover while the potassium content acts as a control for the measurement as its values should not change between samples.

4

Single cell characterization

This section will detail all the measurements that were done to characterize the parameters of the cell and the electrolytes. All measurements in this section were performed on a single cell using a heat bath to control the temperature. The data collected here would be applied to the full system in order to get optimal efficiencies and power outputs. As mentioned in the methodology all measurements were performed using a delayed alternating current. An example of this method can be seen in figure 4.1a. From this measurement data points were collected and then transformed into the desired parameters. It also shows that the measurements contain minor fluctuations which are the result of measuring errors. The most commonly measured parameter, resistance, can be from the I-V curve in figure 4.1b. Using the equilibrium data from the measurement, the resistance is calculated from a linear fit. All measurements shown here were done at a flow rate of 1 mL/s (residence time of 6.93 s) and an inter-electrode distance of 1.6 mm unless stated otherwise.

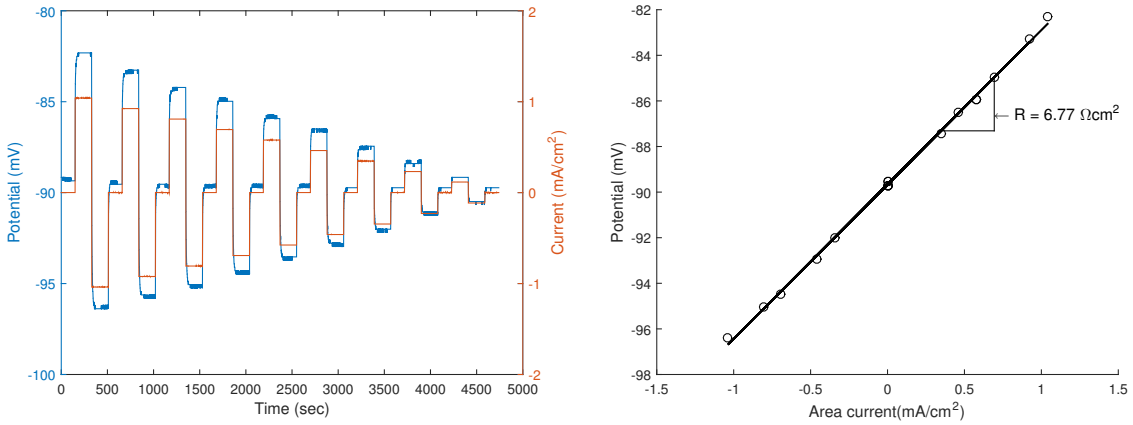

(a) (b)

Figure 4.1: (a) A figure showing how the measurements were performed. 18 different currents were applied to the cell and their response was measured. This data was then used to acquire various parameters. (b) The result of taking the equilibrium data points and performing a linear fit. the resistance is then equal to the gradient of the obtained curve. This measurement had an r^2 value of 0.998 showing a very good linear fit as would be expected. This resulted in a resistance of 6.77 Ωcm^2 for this measurement. These measurements were performed with test composition 6.

4.1. The Seebeck coefficient

As stated in section 2.2.1 the Seebeck coefficient determines the thermo-electric properties of a material. Therefore it is the key parameter to investigate as plays a large role in determining the viability of a design. Before experiments were done, Bleeker made estimations and predictions on the Seebeck coefficient of the electrolytes used in this thesis. While the $Fe(CN)_6^{3-}/Fe(CN)_6^{4-}$ couple has been established in literature to have a Seebeck coefficient of -1.4 mVK^{-1}, less was known about the coefficient of the I_3^-/I^- couple. As es-

tablished by equation 2.3 this coefficient is dependent on the entropy change during the reaction, but for the I_3^-/I^- couple it proved difficult to get an estimation as the reaction was not a straightforward single electron reaction. Thus the coefficient was determined experimentally, which resulted in a value of +1.05 mV K^{-1}.

Based on equation 2.7 this would result in full cell coefficient of +/-2.45 mV K^{-1}. Bleeker tried to determine the accuracy of this number but only managed to do a few experiments, which brought his final value at 2.33 mV K^{-1}. This is not the predicted value and the deviation might be a result of leakage and subsequent cross-contamination of active species as well as different operational concentrations.

The Seebeck coefficient was determined by calculating the gradient after measuring the OCV at various temperatures. The results of these measurements can be seen in figure 4.2. For the second measurement in figure 4.2a this yielded a Seebeck coefficient of -2.45 mV K^{-1}, which is an agreement with the theoretical value. Due to these measurements taking a long time to perform, they were spread over multiple days. This allowed for the solutions to degrade thereby decreasing the concentration. A decrease of the active species concentration has an effect on the Seebeck coefficient, where a higher concentration/purity results in a larger coefficient. This validated the work done by Bleeker, but as can be seen from figure 4.2b the values changed when different electrolyte concentrations were used.

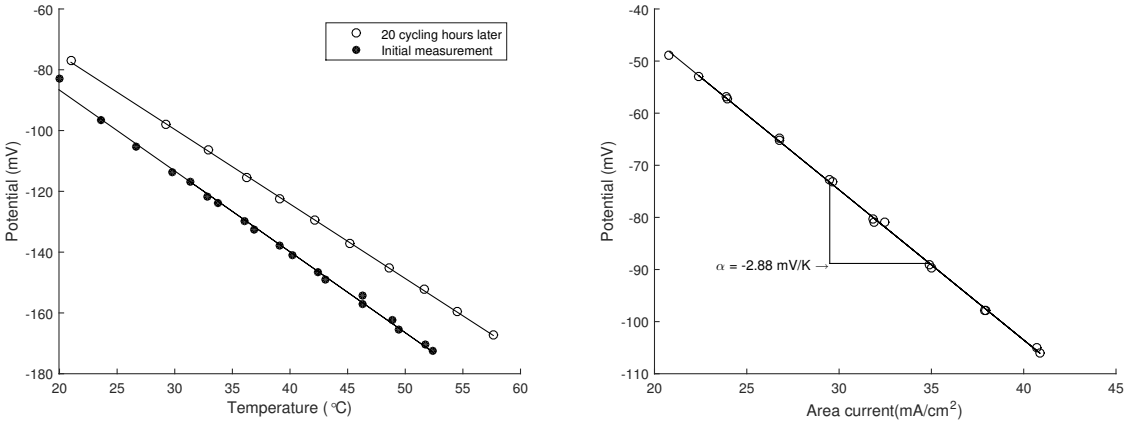

(a) Seebeck coefficient using test comp. 1

(b) Seebeck coefficient using test comp. 6

Figure 4.2: Plots showing the relationship between the temperature and the OCV. (a) A plot showing the data points acquired for the Seebeck coefficient for test composition 1 with the initial measurement heated and cooled with α = -2.65 mV K^{-1},r^2=0.997 and giving data-points 2 weeks later(21 cycling hours) with a α = -2.45 mV K^{-1}, r^2=0.999. (b) Measurements for the Seebeck coefficient using the electrolytes of test composition 6. This yielded α = -2.88 mV K^{-1}, r^2=0.999.

As can be seen in figure 4.2a the absolute potential as well as the Seebeck coefficient change over time. This means that it is not independent from degradation and apparently the reaction entropy is dependent on the concentration of the electrolyte. This would also explain the observation that the Seebeck coefficient decreases when a higher concentration of active species is used. Figure 4.2b shows the relation for the electrolyte of test composition 6 (the highest concentration). This yielded a Seebeck coefficient of -2.88 mV K^{-1}. This is interesting as for most solutions it has been shown that the coefficient gets lower at higher concentrations. Apparently some other effects are at play which shows more fundamental knowledge of the behaviour of the Seebeck coefficient is needed.

The coefficient obtained in this thesis is high for an aqueous electrolyte. At -2.88 mVK^{-1} it is one of the highest recorded values for aqueous electrolytes that have been found so far in literature. The only mentions of higher values are for systems that have added solvents or stabilizers, and even then the highest reported value for aqueous electrolytes is only 0.02 mV K^{-1} higher[39] than the coefficient obtained in this work. Fortunately, the current work does not preclude the use of any of these additives and therefore it is very likely that an even higher coefficient could be obtained. The high coefficient also gives another advantage as it will be easier to get high energy efficiencies based on equation 2.8.

During these measurements it was also apparent that the equilibrium potential was far off from the potential that was determined using cyclic voltammetry. As mentioned in section 2.1 this potential was expected to be -0.22 V. The variation of this value is explained by the Nernst equation because at higher concentrations the activity coefficients deviate from unity and therefore increasingly influence the equilibrium potential. This can also be seen in the very different potentials between figure 4.2a and 4.2b as these measurements

were performed with electrolytes with different concentrations.

4.2. Temperature effect

This section explores how the temperature affects the resistance of the cell. In section 2.4.1 it was explained how changing the temperature can influence the resistance. By doing measurements at various temperatures and calculating the resistance, figure 4.2 was made. As can be seen the resistance noticeably drops when the temperature increases. As previously explained, this is the result of an increased ionic mobility. The equation to describe the behaviour of resistance with temperature in electrolytes[46] is defined as follows:

$$R = \frac{R_{ref}}{1 + \theta * (T - T_{ref})} \tag{4.1}$$

where R is the resistance, T the temperature, and θ the temperature coefficient. This equation is hyperbolic which would be expected as the resistance must be an asymptotic function because negative resistance is not possible.

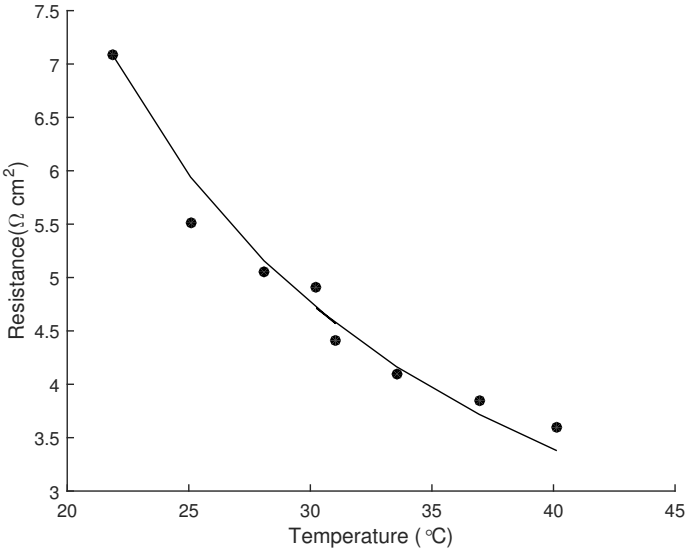

Figure 4.3: A plot showing the trend of resistance with increasing temperature. As can be seen the fitted trend-line lines up somewhat well with the acquired data points with an r^2=0.9640 with a temperature coefficient of 0.06 K^{-1}. Using this coefficient we can extrapolate the resistance value to get an indication for higher temperatures. These measurements were performed with test composition 6.

The data in figure 4.2 shows a somewhat good fit with equation 4.1. The temperature coefficient derived from this fit was determined to be $0.06K^{-1}$. Compared to the data obtained by Mäntynen et al.[46] this seems somewhat high but this can be attributed to the higher concentration used in this work. Using the coefficient obtained from the data, it was predicted that the area resistance to go down from 6.73 Ωcm^2 at room temperature to approximately 1.5 Ωcm^2 at 80°C. This would be very good for the overall efficiency as well as the maximum power output of the setup as a low resistance would increase their respective values. This shows that not only is a high temperature difference beneficial for the potential difference, it also benefits the electrical resistance as the overall resistance will be lower.

4.3. Electrolyte composition

The electrolytes play an important role in the design of the set-up. While the particular species determines the thermo-electric properties, the concentration and counter-ions in the solution play a large role with regards to the conductivity. After investigation it was determined that the ferri/ferrocyanide species had the lowest solubility of all the used compounds[47] (OLI Studio). Therefore it determined the maximum concentration of active species in both electrolytes. Figure 4.4 shows how varying the electrolyte concentration changes the resistance. It clearly shows that at a higher concentration, the resistance is significantly decreased. This is also evident from conductivity charts as no maximum, other than the solubility limit, is obtained when dissolving

the active components.[47] Measurements at other concentrations were not performed as they seemed redundant. Unfortunately this resulted in a limited amount of data-points and thus only a qualitative correlation can be made about the concentration's effect on the resistance.

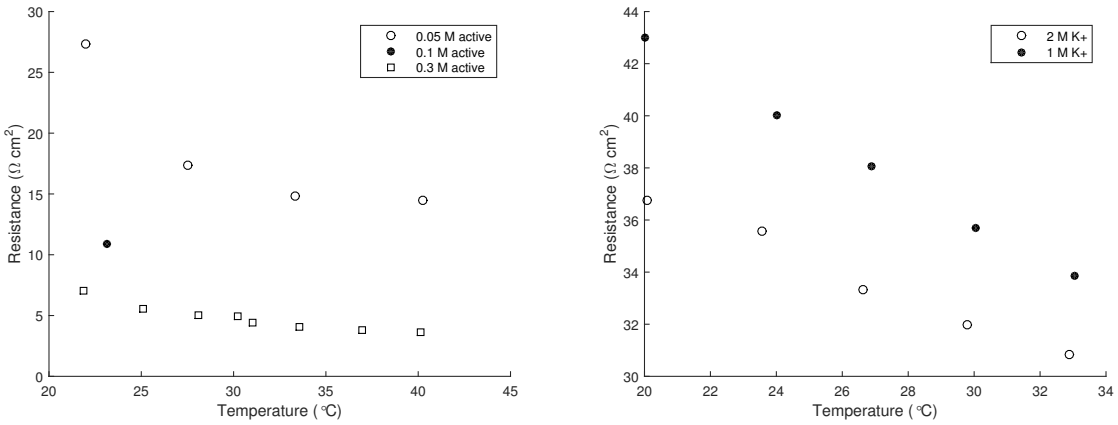

(a) Active electrolyte

(b) Supporting electrolyte

Figure 4.4: Plots for the resistance at varying electrolyte compositions (a) Plot varying the active species concentration with concentrations 0.05 M, 0.1 M, and 0.3 M respectively test composition 4,5, and 6. While the various datapoints may not seem to have the same trend they do but due to the absolute change being different it is not that visible. (b)Plot varying the concentration of the supporting electrolyte concentration with concentrations of 2 M K^+ and 1 M K^+ respectively test compositions 5 and 1. These measurements were performed with an inter-electrode distance of 8 mm which explains why they do not match the values of figure 4.4a.

The first electrolyte parameter that could be altered was the concentration of the active species. As stated previously this change was limited by the solubility and therefore only a few measurements were performed. As can be seen in figure 4.4a, the concentration drops strongly when the concentration increases. Due to the limited amount of concentrations tested, no correlation is visible between the change in concentration and the resistance while for strong electrolytes this trend should be the linear with the concentration. When the concentration doubles to 0.1 M the resistance decrease by 57% but when it increased six-fold to 0.3 M the resistance only decreases by 75%. If the resistance would have changed linearly this should have resulted in negative resistances. The deviation form this trend can be explained by not properly dissolving molecules and well as the changing composition as not all ions have the same conductivity.[47] Equation 4.3 also supports this theory as the concentrations do not change with equal ratios between the various compositions. Therefore the trend does not seem linear as the components have different mobilities thus allowing for non-linear observed behaviour. While the conductivity is related to the ohmic resistance through equation 2.10, the concentration also influences the non-ohmic overpotential as it is non-linearly dependent on the concentration as is demonstrated by equation 4.2. Thus, while it is difficult to state the exact dependency of the resistance on the concentration, it is apparent that increasing the concentration has a significant effect on the resistance of the electrolyte.

$$\eta_{Conc} = \frac{RT}{nF} \ln \frac{C_0}{C_b} \tag{4.2}$$

A second electrolyte parameter that could be changed was the concentration of the supporting electrolyte. While the active species concentration was limited this was not the solubility limit for all salts. The charge equalizing species (potassium) concentration could be increased to make the solution even more conductive and thus decrease the resistance even further. In the current work this meant that potassium chloride was added to the solution.

$$\kappa = F \sum_i |z_i| u_i C_i \tag{4.3}$$

Figure 4.4b shows the results of the various resistance vs. temperature measurements for different supporting electrolyte concentrations. During the measurement with a supporting cation concentration of 1 M

K^+, the results of Bleeker were confirmed as an area resistance of 42.9 Ωcm^2 was found at 20°C which was very close to the data that was obtained during his measurements(44.2 Ωcm^2).

Additionally, figure 4.4b shows that increasing the supporting electrolyte concentration does indeed have an effect on the resistance for a given active species concentration. While this effect is not as pronounced as when the active species concentration is varied, it is still significant. When the concentration of potassium species is doubled, the resistance decreases by 10-15%. this can be attributed to the increased conductivity of the solution however it also possible that decreased migration of the active species play a role due to the migration being performed by the supporting electrolyte. After doing more calculations in OLI Studio, it was established that the concentration could be increased even further up to 2.8 M potassium ions. However, this was not investigated experimentally as this meant that the solution would be very near saturation and thus precipitation could easily occur. Working at this solubility limit could potentially decrease the resistance by a further 5% if the current values are linearly extrapolated and thus if necessary to get a workable overall efficiency or power output, could be implemented.

4.4. Cell design

Section 2.4.1 stated that changes to the cell configuration could change the amount of resistance. It was explained that the inter-electrode distance was decreased by changing the flow spacer. The results of this change can be seen in figure 4.4. Figure 4.4 shows that the area resistance decreases by approximately 60-70% for all measured temperatures while as stated in section 3.1 the inter-electrode distance was decreased form 8.2 mm to 1.8mm(approximately 80% decrease). Based on equation 2.10 a linear dependency is expected but the results do not match this relationship. It is not possible to state the exact relationship between resistance and thickness due to only having 2 data points however given more data it will likely conform to the linear relationship. There is also a non-ohmic component to the change in thickness as it significantly increased the liquid velocity. Equation 4.4 shows that the overpotential is dependant on the velocity (Q/A) and thus for more representative data the velocity should have been kept equal. Of all the parameters that were tested in this thesis, the thickness had the greatest impact on the resistance and it is possible to make the cell even thinner which could decrease it even further. A downside of this decreased thickness, is an increased pressure in the system which requires better connectors and sealing to prevent leakage. The fact that the cell can be made this thin is also beneficial in other ways as it reduces the spacial footprint as well as the amount of material that is needed and therefore the overall cost.

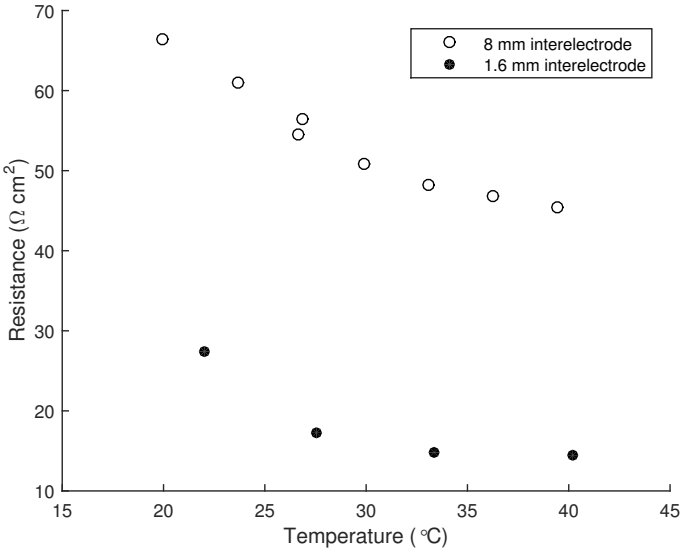

Figure 4.5: A graph showing how the resistance changes with the cell thickness. Both these measurements have an active species concentration of 0.05 M and potassium ion concentration of 2 M (Test composition 4). The resistance significantly drops when inter electrode distance decreases.

Another part of the cell design that was changed, were the electrodes. During measurements it was noticed that the carbon electrodes became porous over time which resulted in leakage and damage to the wiring.

To combat this leakage a different electrode material was chosen. This material had to adhere to all the design parameters which resulted in titanium being chosen as an electrode material. During initial testing it became clear that a side reaction was occurring as very high overpotential was measured. After these measurements the titanium plate had changed colour. The analysis of what caused this change can be found in section 6.2. In the end the graphite electrodes were still used and just replaced after every measurement series as for the current work this was an easier and cheaper strategy than buying electrodes that will not degrade.

4.5. Flow rate

Another critical parameter that was evaluated was the flow rate of the electrolyte. The flow rate can influence the resistance by feeding more unconverted ions to the electrode surface and therefore decrease the boundary layer. Additionally, it will have quite a large influence on the efficiency as pumps can be quite energy intensive and inefficient. Therefore it is important to find the trade-off flow rate where the gains in reduced power consumption are balanced by the increase in resistance. Figure 4.5 shows how the resistance varies with the flow rate.

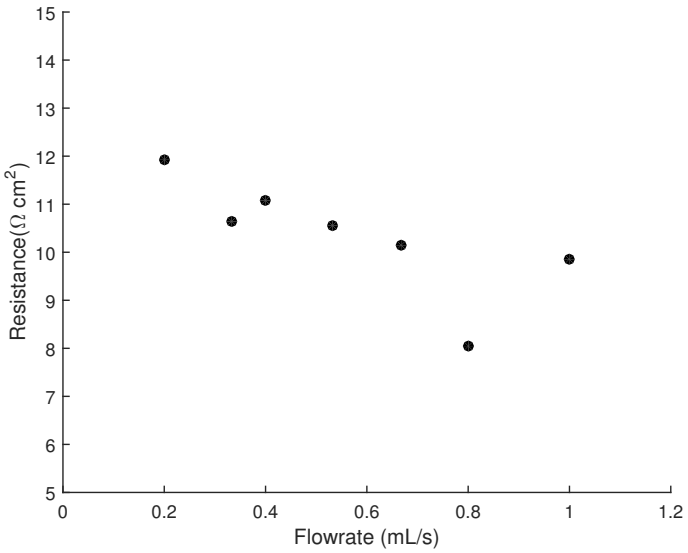

Figure 4.6: A graph showing the relationship between the flow rate and the resistance. As can be seen the resistance decreases with the flow rate. The relationship looks linear with a few outliers in the data however it is not expected to continually decrease and is more likely to be hyperbolic like the temperature relationship. This is confirmed by equation 4.4. These measurements were performed with test composition 5.

The resistance in this figure should decrease according to equation 4.4 for a higher flow rate.[48] This equation shows that the overpotential and thus the resistance should change with the logarithm of the flow rate with higher flow rates causing a decrease and this trend can be seen slightly in figure 4.5. The change in resistance is 1.2 Ωcm^2 (20% decrease) for a five-fold increase in flow rate. This acquired data points also show slightly logarithmic behaviour as their change becomes smaller with higher flow rates. Even though the relationship should be logarithmic, it looks slightly more linear than logarithmic so for full confirmation of this behaviour a larger range of flow rates (in particular low flow rates) is necessary. Nonetheless this equation also supports the idea of a trade-off between flow rate and decreased resistance because a very large increase in flow rate only results in a minor decrease in concentration.

$$\eta_{Conc} = \frac{RT}{nF} * ln\left(1 - \frac{i}{1.6 * 10^{-4} * \frac{Q}{A} C_b}\right) \tag{4.4}$$

This power consumption was measured with a power meter in the pump's electrical outlet. The results can be seen in table 4.1. It shows that the percentile increase in consumption is lower that the decrease in resistance but the absolute values are much higher than any amount of power we could produce with his system. Therefore it was more appropriate to calculate the power consumption using the Hagen-Poisseuille

equation. The pressure drop over the cell was calculated using an equation derived by Da Costa et al.[49] which can be found in appendix A. Together they result in equation 4.5.

$$P_{theo} = \left(\frac{8\mu l Q}{\pi r^4} + \Delta P_{Cell}\right) * 2Q \tag{4.5}$$

As can be seen in table 4.1 the true power consumption is much higher than the theoretical value which highlights how inefficient the current pump is. From the calculated values it can be seen that their effect on the efficiency of the system is very small. This is mostly due to the relatively low flow rate. The system has also been minimized in terms of pumping length/distance which results in a smaller required pumping power. While this value is theoretical is does give a better indication of the pumping power requirement than the values the current pump provides. The true value will undoubtedly be higher than the theoretical value due to losses as well as requiring other electrical systems to operate but should not be as high as the currently used pump.

Table 4.1: A table showing the flow rate and the accompanying power consumption based on a radius of 3 mm, a viscosity of $1.08 * 10^{-3} Pa * s$, and a pumping distance of 10 m. It shows that the theoretical pumping power is a few orders of magnitude smaller than the currently consumed power. The residence time can be calculated by dividing the above electrode volume by the flowrate. Here the volume is calculated by multiplying the height ($800\mu m$) by the area ($\pi * 5.25^2$).

Flow rate (mL/s)	**Residence time (s)**	**Theoretical pumping power (W)**	**True pumping power(W)**
1.33	5.2	$2.1 * 10^{-2}$	16.3
1	6.9	$9.7 * 10^{-3}$	13.6
0.66	10.4	$3.3 * 10^{-3}$	12.3
0.33	20.8	$5.8 * 10^{-4}$	9.2
0.08	86.6	$2.2 * 10^{-5}$	7.9

4.6. High current

While all the above measurements were conducted between 10 and 90 mA, these values might not be optimal. Therefore the cell was tested at higher currents to assess the behaviour at these currents and to find the limiting current. If this limiting current is very low, a high power output cannot be attained. To assess the maximal operational current it was slowly increased by 20 mA at a time until a threshold was reached where the resistance is no longer linear as diffusion limitations will be reached. A higher power output is also coupled to a higher current through equation A.9 where a maximum occurs due to increasing loss to resistance. This tradeoff point will determined experimentally in chapter 5. The results of the high current measurements can be seen in figure 4.6.

The measurements showed that the current can easily go up to 850 mA (+/- 10 mA/cm^2). Measurements were done at even higher currents but at that point the solution had degraded (due to being 3 days later) to some extent and they did not fit nicely with the shown data anymore. The plot for these data-points still show linear behaviour only at a different specific resistance. From further data that was obtained, we can assume that the limiting current is at about 1.2 A (+/- 14 mA/cm^2) as at this current the response became more erratic with potential spikes in the output which were possibly related to a temporary lack of active species. The limiting current density was also calculated using the formula given in equation 4.6. To be able to use this equation we determined the species with the lowest diffusion coefficient as it would be the limiting species. It was found that the triiodide species had the lowest diffusion coefficient at $8.6 * 10^{-10} m^2/s$.[50] Next we had to determine the diffusion boundary layer. It was assumed that at the highest this value would be 400 micrometers. Filling in the equation for these values gives a limiting current of 1.08 A. This is slightly below our acquired value and thus the diffusion layer is likely to be smaller than estimated.

$$i_{lim} = nFA\frac{D_{lim}}{\delta}C_{lim} \tag{4.6}$$

While most results were obtained at low current densities this leaves the question if they will also still apply for higher current densities. It is assumed that they will translate to higher current due to the stability of all the performed measurements.

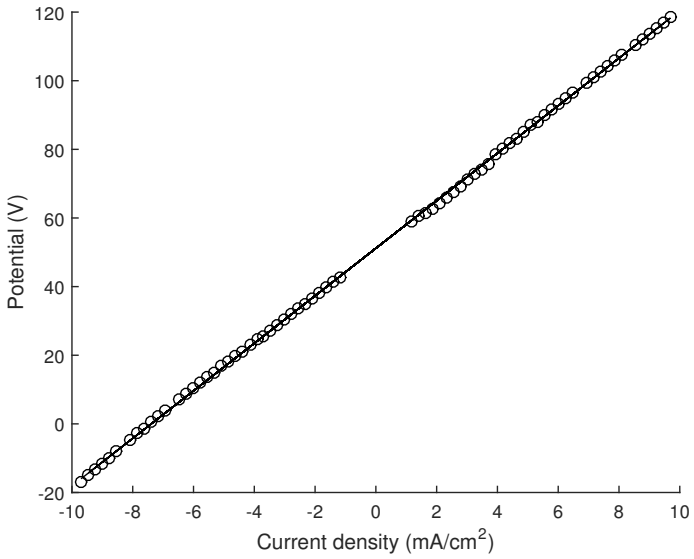

Figure 4.7: A plot showing the potential a higher current densities. High currents were reached without straying from the linear regime. the linear relation between the shown values is the resistance which for this measurement was 6.92 Ωcm^2 with r^2=0.999. These measurements were done with composition 6 at 20°C.

4.7. Impedance

To find out what the true ohmic resistance was, impedance measurements were performed. These measurements were performed for a current ranging from +/-100-1000 mA. Figure 4.7 shows the results of these measurements. As can be seen the current does not have a large influence on the ohmic resistance as the recorded value is almost the same for all measurements at 43 mΩ (3.72 Ωcm^2).

This is an interesting result as the ohmic resistance was also measured during the high current measurements. It could be determined by measuring the potential response when the current was removed from the sample. When this potential was normalized with the current it gave an ohmic resistance of 65 mΩ (5.63 Ωcm^2). This is strange as it was expected that the values would be identical. A possible reason for the mismatch could be the time resolution of the measurement. While the impedance measurement was averaged between 1000 and 10000 Hz, the very first measurement during the high current measurement was only done after 0.05 seconds(20 Hz). This would indicate that within this time-span the non-ohmic effects have already started playing a role.

Based on these results, it can be concluded that the ohmic resistance is at least half of the total resistance. The results also show that there are still some gains to be made as the ohmic resistance can still be decreased. For future cell designs, a zero gap cell could be built as the majority of this resistance is likely due to the inter-electrode distance. The main source of the non-ohmic resistance (14.9 mΩ (1.29 Ωcm^2) based on the high current measurements but is likely to be larger as explained in the previous paragraph) is caused by diffusion limitations. For the current cell design, the non-ohmic resistance could also be decreased, because as mentioned in section 4.5, the flow rate can be increased which will decrease the diffusion boundary layer and thus the non-ohmic resistance as well.

4.8. Optimal operational conditions

Using all the data presented in this section the optimal conditions for the current setup can be found. These conditions will be used for all the measurements with the full setup as they are most likely to give the best power outputs and efficiencies. It has also become evident that there are many factors which can influence the cell resistance. The optimal conditions are as follows:

- Concentrations: As high as possible, in the current work 0.3 M for all active species and 2 M for potassium ions
- Current: Depending on what current delivers the maximum power but shown to be stable up to 1 A

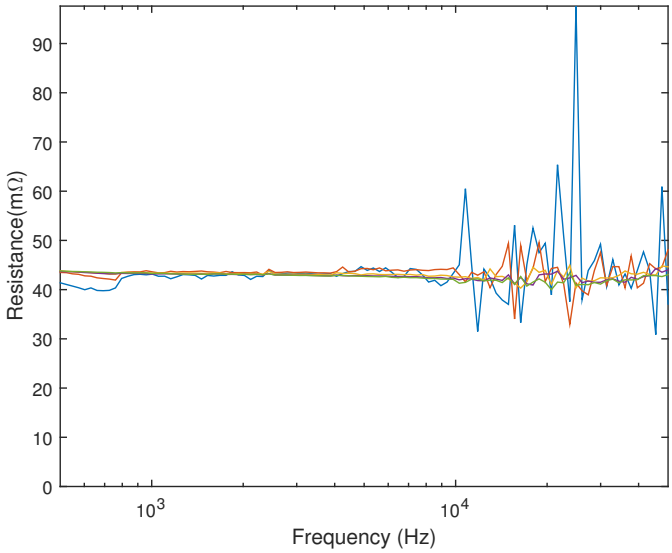

Figure 4.8: A plot showing the impedance measurement form 500 to 50000 Hz. While measurements were done every 50 mA this graph only shows the responses for 100(blue), 200(orange), 400(yellow), 600(purple), 800(green) mA. The regime without the noise (1000-10000 Hz) is of interest as this is where the ohmic resistance can be measured. The average value for all this data in the frequencies of interest is 43.1 mΩ. These measurements were performed with test composition 6.

- Temperature: As large a temperature difference as possible, in the current work aimed at $\Delta T = 60°C$
- Design: As thin as possible with optimal electrode kinetics even though for the current work these kinetics are thought to play a minor role
- Flow rate: A trade-off between decreased resistance and increased pumping power, for the current work 1 mL/s has been chosen as a flow rate

These operational conditions conclude this chapter and bring us to the next chapter which will test the true efficiency and power output of the thermo-electrochemical flow cell setup. We have shown a high Seebeck coefficient coupled with a relatively low cell resistance as well a theoretically functioning continuously operating flow cell. Based on all the information the full setup is expected to perform well.

Using the data available we can make some predictions on the optimal power and efficiency. With equation 2.9 and the obtained seebeck coefficient(2.88 mVK^{-1}) and resistance(8.52 Ωcm^2 which is the sum of the cold cell and the extrapolated value for the hot cell at the highest concentrations) we can assess the maximum power. This results in a $P_{Max}m^{-2}$ of 8.66 Wm^{-2} at a ΔT of 60. This value can then be normalized with the temperature difference which results in a $P_{Max}m^{-2}(\Delta T)^{-2}$ of 2.40 $mWm^{-2}K^{-2}$. While these values might not seem impressive, they do show the potential this setup has. Zhang et al.[37] published a paper with some of the highest values ever recorded and while the current work does not have the highest power density, it does have a temperature normalized power density almost 1.5 times higher than the highest value they recorded. This shows that the current setup has potential when it comes to power output and can compete with some of the more advanced thermo-electric cells.

Now that we know that the power density is, we can make an attempt at calculating the absolute and relative heat-to-power efficiency. The energy output for this equation will be the P_{Max} and the energy inputs are the pumping energy and the heating energy. The calculated P_{Max} for the current setup is 75 mW. The pumping power as mentioned in section 4.5 will be the theoretical pumping power and not the actual measured values due to the actual values being several orders of magnitude larger due to an extremely inefficient pump. This resulted in a pumping power of 3 mW. Finally the heating energy has to be estimated. Due to a lack of data we will use the heat capacity and density of water(4.2 J/gK and 1 g/mL respectively) as they will be of the same order as the true values. The ΔT is very dependant on the efficiency of the heat exchangers and effectivity of the insulation. For this calculation it will be assumed to be 10 degrees which is the value that was also used for the heat exchanger sizing. This results in a required heating power of 84 W. This is a fairly high value but improved heat exchangers can drastically lower this value. These values result in an overall absolute

efficiency of 0.09%. Using this efficiency we can calculate the efficiency relative to Carnot which comes out at 0.53%. These are both very low values and are much lower than initially expected. As can be seen the main cause of the low efficiency is the energy required to heat the liquids. This could be minimized with a very high rate of heat recuperation(>98%). On the other hand while a high efficiency is important, a high power output is more important as it was already assumed that the heat input is waste and would therefore cost energy to discard. Another option would be to use a lower flow rate or split the current flow over multiple cells to achieve a higher power output with the same heating power.

5

Full setup operation

This chapter will contain the results of full setup operation. It will be assessed by a variety of parameters which were mentioned in chapter 2. Aside from the power and efficiency of the setup, the custom designed heat exchanger will also be evaluated. Furthermore any problems that were encountered will be assessed. All measurements in this section were performed using an active species concentration of 0.3 M (test composition 6).

5.1. The thermo-electrochemical flow cell

After building the setup described in figure C, some problems occurred during initial testing. It was discovered that the heat exchangers had to be filled prior to testing as the air within them could not be removed due to their positioning. It was also discovered that at a flow rate of of 1 mL/s the pressure buildup over the cells was large enough to cause an integrity failure within the connectors. Therefore the flow-rate was lowered to 0.33 mL/s. After these operational changes the entire cell worked as designed with liquid flowing through all components without problems at room temperature. Upon heating a similar pressure problems occurred which resulted in a large pressure drop at high temperatures. It was concluded that this was caused by thermal expansion of the components at higher temperatures. After investigation is was discovered that PTFE has a thermal coefficient of $120 * 10^{-6} m/(mK)$[51] which is an order of magnitude higher than the coefficient for the steel screws($11 * 10^{-6} m/(mK)$). Given the average hot temperature of 62°C this mean that the cell could expand up to 200 μm inward. This resulted in a smaller internal flow area and smaller in- and outlets which then resulted in an increased system pressure. Despite this pressure issue, the setup worked but required increased monitoring to avoid leakage.

5.2. Cell performance & efficiency

This section will analyze the various parameters by which the setup can be evaluated. In particular the performance and efficiency will be calculated but also some secondary parameters relating to redox flow batteries will be evaluated. The equations and criteria that it will be used to evaluate the setup can be found in chapter 2.

As mentioned in section 2.3, this setup functions somewhat similar to redox flow batteries and could therefore also be judged by the same parameters. One of the most important for a redox flow battery is the energy density as the volume of the system is the main limiting factor for it. For the current system using test composition 6 this energy density was determined to be 1.32 Wh/L. This is not a very high value as redox flow batteries have an energy density of an order of magnitude higher.[52] This is not surprising as the concentration of our active species is somewhat low compared to real redox flow batteries and therefore our setup can hold less energy per liter. Another parameter that was mentioned was the state of charge. This is an important parameter as it is measure of how efficient the electrolyte is used. For the current setup it was heavily dependent on the applied current and residence time. Based on the obtained data for the maximum power at a temperature split of 43.5°C, the maximum current was 1.35 mA/cm^2. With a flow-rate of 0.33 mL/s, the electrolyte had a residence time over the electrode of 20.8 seconds. Using these values we could calculate the conversion of ions per pass. This resulted in a conversion of 1.2% of the ions per pass through the cell. Assuming we have a split of 50% (equal amounts of both redox species) we cycled between 50 and

51.2%. This is not very high but it does benefit the concentration difference as the concentration will remain high on average. The non-ohmic part of the overpotential is dependant on the difference in concentration between the bulk and the electrode and thus staying at approximately 50% will minimize it while keeping the difference relatively high. This state of charge cycle is somewhat poor for a redox flow battery but is most likely better for our application. Therefore the parameters by which redox flow cells are judged are not very useful to judge thermo-electrochemical cells.

5.2.1. Power performance

By running the chronoamperometric scheme described in section 3.2 a power vs. current curve could be constructed. Figure 5.1 show these curves for various temperature differences. As can be seen the curves are parabolic which is to be expected and at some point they produce negative power outputs. This means that at these currents the ohmic loss becomes greater than the power output which results in a net loss of power. This figure also shows that when the temperature difference is 0, no net power can be obtained from the cell due to the potentials of each cell cancelling each other out. Due to the parabolic nature, a maximum could also be calculated. By doing a parabolic fit and taking the derivative with respect to the current as shown in appendix A the maximum power output at a certain temperature difference can be obtained. For this research the maximum power was shown to be 5.15 mW (0.59 Wm^{-2}) at a temperature difference of 43.5°C. Compared to the expected value of 8.66 Wm^{-2} the cell has significantly under-performed. Additionally the desired temperature difference was also not achieved and the the temperature normalized power density also fell short at 0.32 $mWm^{-2}K^{-2}$. The explanation for this underperformance is relatively straightforward as after analysis it became apparent that both the Seebeck coefficient and the resistance were far from the desired values.

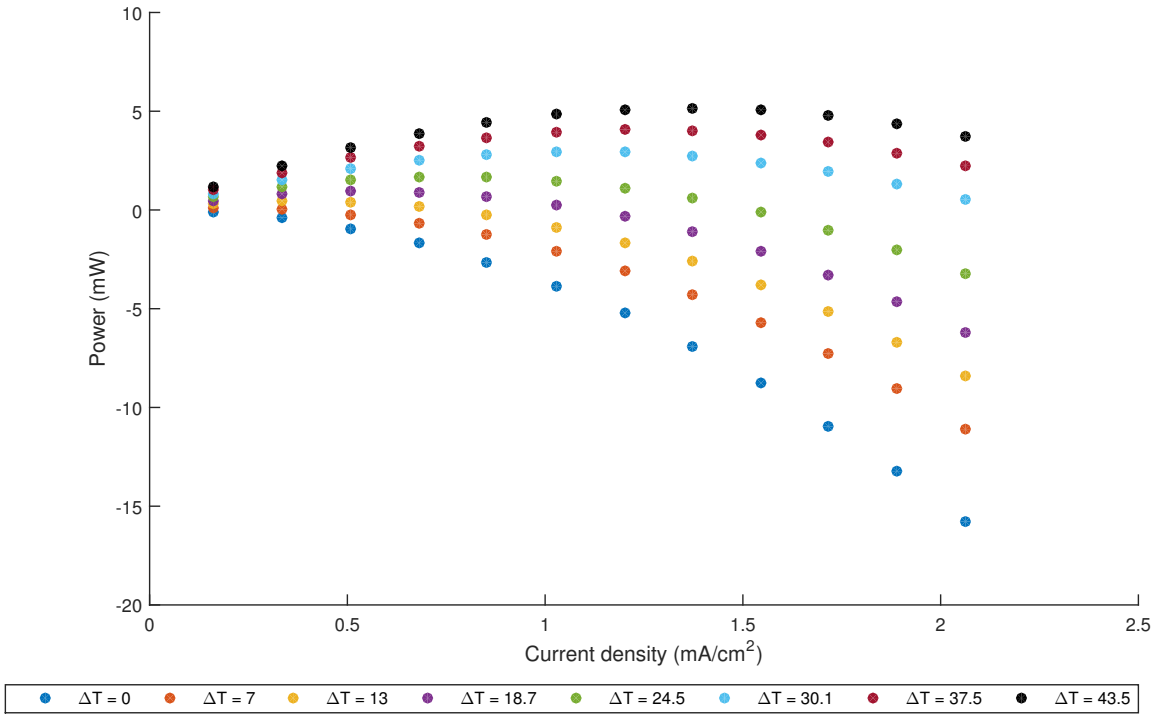

Figure 5.1: A plot showing the change of power with increasing current for various temperature differences. As can be seen the power curve increases with an increasing temperature starting out at only negative power (only consumption) and moving to positive power at higher currents (net production) with a higher temperature difference between the cells. All the curves fit a parabolic trend with a $r^2 > 0.999$ which is expected for power curves based on the potential and current.

Figure 5.2a shows the OCV as a function of the temperature difference. The resultant coefficient is only -2.02 mVK^{-1} which is almost 30% lower than the value which was expected from the results in chapter 4.1. To

find the exact cause, more data needs to be available on the behaviour of the Seebeck coefficient, however we can speculate about the cause. One possibility is the cross-contamination of the electrolytes. Due to extended contact times it is possible that they have significantly diffused through the membrane which would cause a decrease in concentration of the active species in both electrolytes but also cause the wrong redox reaction to occur at the electrodes to an extent that the measured overall coefficient becomes a mixture of the individual coefficients. This crossover and concentration drop was analyzed in chapter 6. Nevertheless the obtained coefficient is not low in the relative sense as it still high for aqueous electrolytes.

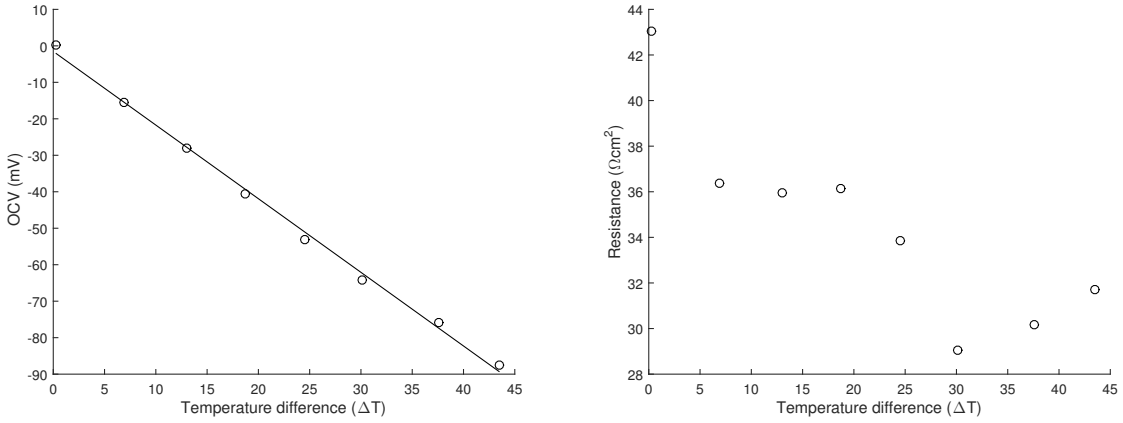

(a) Seebeck coefficient data

(b) Resistance data

Figure 5.2: (a) A plot showing the change of the OCV with temperature. As can be seen the plot is linear which is expected. This resulted in a Seebeck coefficient of 2.02 mVK^{-1} with an r^2=0.997 indicating a proper linear fit. (b) A plot showing the variation of the area resistance with the temperature difference between cells. As can be seen there is no obvious correlation with the area resistance hardly changing and sometimes increasing with temperature whereas only a decrease is expected.

Figure 5.2b shows the change in resistance with respect to temperature. While not the exact same temperature-resistance correlation as in section 4.2 will be found, it is unlikely that the resistance only changes minimally with such a temperature increase with no apparent correlation. It could also be caused by the drop in concentration in the electrolytes, however based on the results of section 4.3 the concentration will need to be decreased by 50% to achieve such an increase in resistance so it is unlikely to be the cause. It also strange that the resistance increases with increasing temperature for the last three measurements even though the opposite phenomena should occur. Also the strong drop between the first two measurements and the fifth and sixth measurement are odd as the change should be more gradual based on equation 4.1.

Upon further investigation it was determined that a resistance of 0.26 Ω (0.1 Ω was expected whereas 0.36 Ω has been measured) had been introduced into the electrical loop. So the various components were tested and it was noticed that the contact to make the electric loop between the two cells was not very good and the slightest movement already had an impact on the measured resistance. This was possible in the full setup because it contained more wiring which was not as well connected in comparison with the single cell experiments. This can be seen in section 5.2.2 where the wiring was slightly moved during the measurement. Due to the order of magnitude of the resistance, it is very likely that the smallest disturbance could have a large impact. It would also explain why the temperature has a negligible influence as the outer wiring was not heated and therefore would not change with an increased electrolyte temperature. Its relative magnitude is so much larger that the decreased resistance as a result of an increased temperature would only have a minimal effect. Another possible cause of the increased resistance could be fouling of the electrode and the membranes(deposition of Prussian blue or iron oxide and degradation due to corrosion caused by the iodide solution). As can be seen in appendix D there is significant damage and fouling which could make the kinetics slower or just increase the resistance by adding an extra layer to diffuse through.

While the desired temperature difference was not obtained during this work the power curves do allow us to calculate what the maximum power output would have been at this temperature difference. This can be done by plotting the maximum power vs square of the temperature difference. Based on equation 2.9 this should result in a linear relationship. This result of this calculation can be seen in figure 5.3. As can be seen the correlation is linear. Using the corresponding equation it can be calculated that the maximum power output at a temperature difference of 60°C would be 10.1 mW. This would be equivalent to a power density of

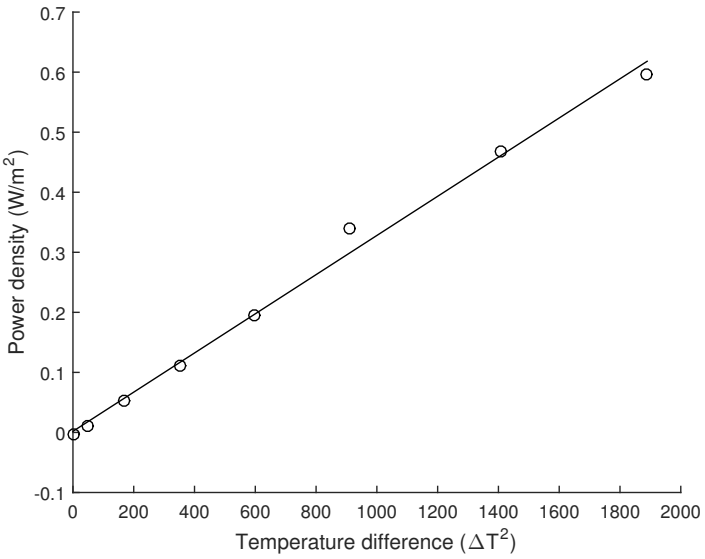

Figure 5.3: A graph showing the relation between the maximum power and the square of the temperature difference. As can be seen this is linear behaviour which is expected. It also shows that the power increases very strongly with an increase in temperature difference. The gradient of the linear regression is 0.00028 $Wm^{-2}K^{-2}$ with an r^2=0.993 indicating a good fit.

1.17 Wm^{-2}. Unfortunately this does not change much about the temperature normalized power density as it would still have a value of 0.33 $mWm^{-2}K^{-2}$. From the linear correlation the Seebeck coefficient could also be extracted as the gradient would be equal to $\alpha/4 * R_{total}$ based on equation 2.9. This resulted in a Seebeck coefficient of 1.91 mVK^{-1} which is very close to the actually measured value. This shows that the equation can be used to accurately describe and predict performances of a thermo-electrochemical flow cell.

Even though the setup underperformed its (normalized) power density is higher than many other investigated cells. Compared to other research[31,32,53] we are on the same level or already higher in terms of (normalized) power density(often 3 mWm^{-2} and 0.03 $mWm^{-2}K^{-2}$ or lower). This only goes to show how good the setup would have been in terms of power production if the predicted values had been reached. Therefore it is unfortunate the both the Seebeck coefficient and resistance were respectively lower and higher than expected as with only one of the two different, a much better performance could have been obtained.

5.2.2. Efficiency

The efficiency of the cell was also assessed. Using an equation of energy out (power output) divided by energy in (heat and pump input) we could determine the absolute efficiency and then also compare it to the efficiency relative to Carnot efficiency. As mentioned in section 2.2.2 the Carnot efficiency is relatively low due to the limited temperature difference between the hot and cold cell. This is not beneficial for the overall efficiency as it is difficult to reach the Carnot limit. It was also discussed in section that the main limit seems to be the amount of heat added and not the theoretical pumping power. Therefore extra thermocouples were added before and after the heat bath to determine the true amount of thermal energy that was added.

Table 5.1: An overview of the various parameters that were used to calculate the efficiencies. It gives the comparison between the predicted theoretical values and the values that were actually measured.

	P (mW)	$Q_{Heating}$ (W)	Q_{Pump} (mW)	$\eta_{Absolute}$ (%)	η_{Carnot} (%)	$\eta_{Relative}$ (%)
Theoretical	75	84	3.2	0.09	16.99	0.53
Measured	5.15	127.9	0.6	0.004	12.95	0.03

Using the same assumptions made in section 4.8 about the heat capacity and density we could again calculate how much energy we needed to heat the system and to operate the pump. In the previous section we already found that the maximum power output is 5.15 mW. The pumping power was calculated in the same way as section 4.5 only for a flow-rate of 0.33 mL/s. This resulted in a theoretical pumping power consumption of 0.6 mW. From figure 5.6 we can see that in the heat bath the liquid was heated by 46°C.

This results in a heating power requirement of 127.9 W. Once again the heating power required is orders of magnitude larger than the other energy variables. These values resulted in an efficiency of 0.004%. This is very low value and also much lower than the efficiency calculated in section 4.8. This low efficiency is caused by the low power output and poor heat management which caused a much larger amount of heat to be added to the electrolytes than was anticipated. The efficiency was then compared to the Carnot efficiency for the acquired temperature difference. The Carnot efficiency for the current setup at maximum power output is 12.95%. This means our relative efficiency comes out at 0.03% versus Carnot. Once again this is a very low relative efficiency. All these results show that the current design requires significant changes to increase both the efficiency and power output. While the relative efficiency is low, it is of the same order of magnitude as a large amount of thermo-electrochemical setups.[53] However these efficiencies are all for normal thermo-electrochemical cells and more representative data comes from Gao et al.[54] which shows that our efficiency is several orders of magnitude lower than comparable systems.

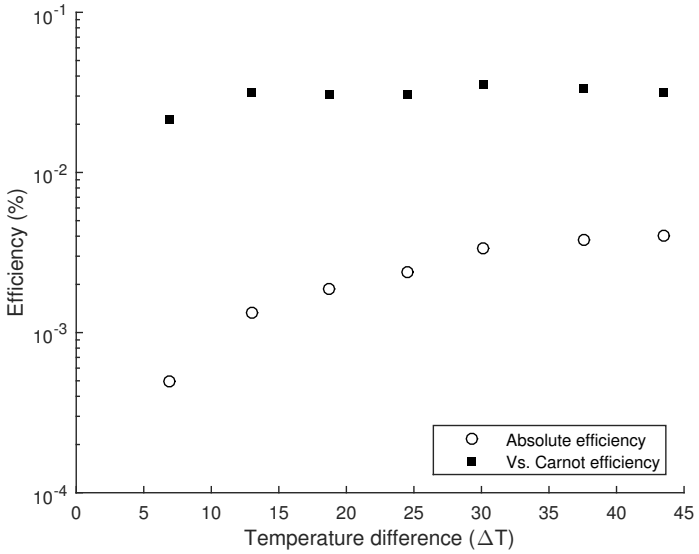

Figure 5.4: A figure showing both the absolute and relative efficiencies at various temperature differences. As can be seen the absolute efficiency increases with the difference whereas the relative efficiency stays approximately the same. The values of both efficiencies are very low being far below 1% efficiency which shows that the current setup is not very efficient and will require some upgrades to become economical.

Figure 5.2.2 shows the change in efficiency related to the temperature difference between the 2 cells. As can be seen the setup gets more efficient with a higher temperature difference. This is caused by the fact that the power increases with the square of the temperature difference while the amount of heat input required only increases linearly. Therefore the system becomes more efficient at high temperature differences. This can also be explained from a thermodynamic perspective as with a higher temperature difference the Carnot efficiency also increases and therefore it is possible to harvest more electrical energy from the thermal energy. Interestingly this means that the energy efficiency relative to the Carnot efficiency only changes marginally and is almost the same for every temperature difference. This increase in efficiency along with the maximum power show how critical it is to be operating at a high temperature. While relative values might not increase much, the absolute values do which brings the setup a step closer to economic viability. A summary of the optimal conditions for the current design is as follows:

- Concentrations: 0.3 M for all active species and 2 M for potassium ions
- Current: 1.35 mA/cm^2
- Temperature: ΔT = 43.5°C
- Design: As thin as possible with optimal electrode kinetics even though for the current work these kinetics are thought to play a minor role
- Flow rate: 0.33 mL/s

5.3. Setup stability

The stability of the setup was tested to be able to gauge the economic viability aside from the optimal power output and efficiency. While stability will impact both of these as it can be assumed that the performance will decrease over time, it is important to have an indication of how long it takes before the cell performance decrease by a certain percentage. This also relates to section 6.1 where the loss of electrolyte concentration was assessed as it is known that a lower concentration will impact the performance.

The stability was tested by running the system at the maximal power output for an extended period of time. Due to minor temperature fluctuations the power also fluctuated a little which can be seen in figure 5.3. It was run for 3 hours to at least get an indication of the power output stability. From the start there is already a minor discrepancy as it was run at the maximum power current described in the previous section, yet the power output is almost a milliwatt lower even though the measurements were only a few minutes apart. As can also be seen in the figure the fluctuations are relatively large while the temperature fluctuations were not so large. This means that there is something else at play. Particularly interesting is the strong increase in power output at approximately t=3600s. This was caused by a movement of the wiring connecting the cells. While no visual difference was observed it apparently resulted in a better contact with the wiring and decreased the resistance. This would give some credibility to the theory that poor contact caused a high resistance that is not influenced by the temperature of the electrolyte. Also evident from figure 5.3 is that the performance does not decrease over a three hour period but actually increases. While this is not likely it could be caused by minute differences in electrolyte composition as the mixing is possibly not very good within the setup. With a 2 L electrolyte volume and a flow-rate of 0.33 mL/s, the circulation time is 6000 seconds and thus the electrolyte circulated almost 2 times during this measurement. This disputes the mixing problem as no correlation is visible between a single point and a point 6000 seconds later during this measurement.

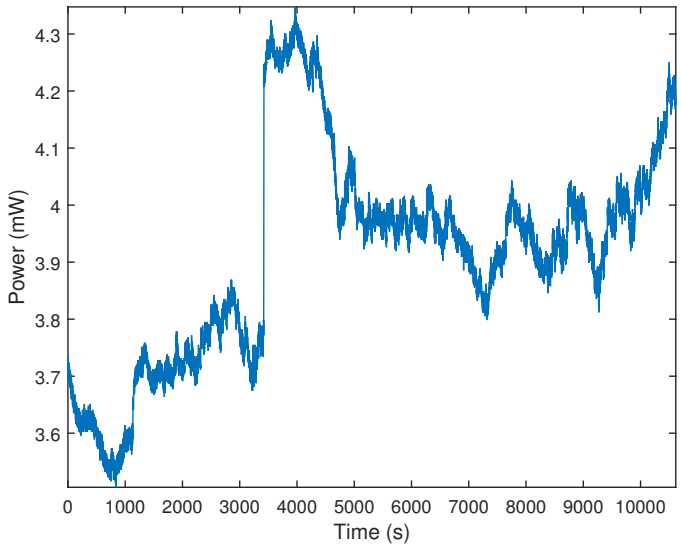

Figure 5.5: A graph showing the power output over time. As can be seen the power output fluctuates quite a lot where the minute fluctuations are small temperature changes, the middle-sized fluctuations are electrolyte related and the very large increase is caused by movement of the wiring. The average power output over the 3 hours of measurement is 3.9 mW.

Taking the average power output over the 3 hours and multiplying it by the time gives us approximately 12 mWh of electrical energy that was produced during the measurement. This is not much and it means that to get anywhere a decent in terms of output the current setup will either need to be significantly scaled up or require a very long time to produce significant amount of electrical energy. For example an average smartphone holds about 10 Wh of electrical energy.[55] This means it will take our setup about 2000 hours to charge it or we need to scale up to $20m^2$ to be able do charge it in an hour. These are quite stunning numbers and show that the current design is far from usable for commercial purposes. On the other hand it does show potential for producing electricity even though the efficiency and the power output of the current setup are low. If it can be improved and we can get the output predicted in section 4.8 for extended periods of time as well as improve the thermal energy retention the design could be commercially viable.

5.4. Heat exchanger

During this thesis the heat exchanger was one of the most critical parts for achieving a high heat-to-power efficiency and it was designed from scratch. As stated in section 3.1.1 a few designs were considered and we ended up with a glass heat exchanger based on a common glass condenser. This heat exchanger was used in counter-current operation in order to use as much heat as possible with the smallest amount of input. Additionally, this mode of operation allowed for the largest temperature difference between in- and outflow. Figure 5.6 gives a profile of the temperature at multiple points in the setup over time. All temperatures remained approximately stable over time except for the outflow of the hot which increased by 0.5°C. This is due to the equilibrium temperature of the cell not being reached yet.

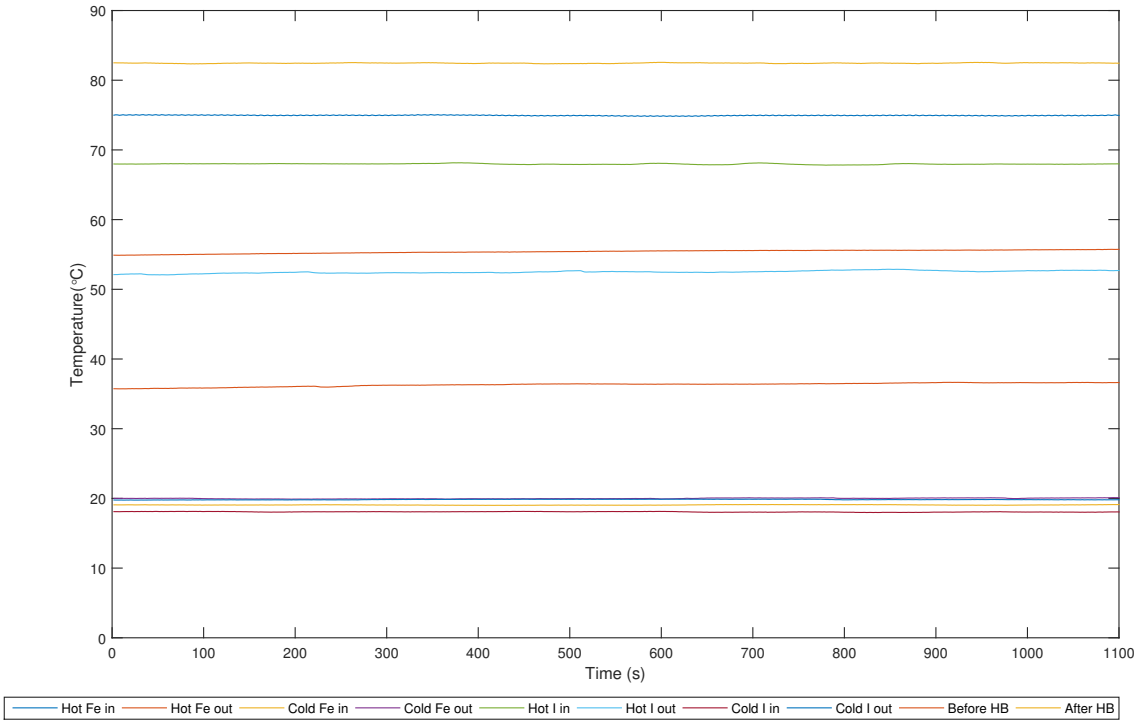

Figure 5.6: The temperatures which were measured during the acquisition of the maximum power for the largest temperature difference between the hot cells. As can be seen the temperatures at the cold cell are all very close to each at approximately 19°C. On the other hand the temperatures at the hot cell are far apart. Interestingly after the hot cell they are closer together than before which shows some degree of heat exchange within the cell. The highest temperature is measured directly after the heat bath (HB) at 82°C. Fe stands for the ferro/ferricyanide side of the cell and I stand for the iodide/triiodide side of the cell. All these recorded values were used for the heat exchanger calculations. The temperature also is very stable over time with only minor fluctuations due to ambient temperature change and due to the peristaltic pump motion. The exit temperatures in the hot cell do show a slight increase of 0.5°C over time but due to using the average temperature in calculations this has little influence.

As can be seen the temperature split is very stable over time. To get these values, the heat bath temperature was set at 90°C and the cold bath at 15°C. The design shows some significant shortcomings and the heat exchanger only raises the temperature by 16.5°C. This is partially due to the low incoming hot temperature due to heat loss but a low operational flowrate does not benefit the heat the retention either . This allowed for the outer liquid to have a lot of contact with the air and thus lose energy. Additionally it is possible that the outer coil did not have any liquid flow as this problem had presented itself during many measurements. When this happened the effective heat transfer area becomes very small thus leading to only heating the incoming liquid a few degrees. These observations would explain the very high temperature approach of 19°C. This is far from the calculated value of 10°C. While this would already be a much better temperature approach, it has become apparent in section 5.2.2 that a temperature approach of just 1°C would be necessary to get an acceptable absolute and relative efficiency.

On top of these slight design shortcomings we also lose quite some heat to the surrounding air. It was attempted to minimize this effect by changing the flow rate but increasing it did not give any advantages. Decreasing the flow rate lowered the temperature split even though the residence time in the heat bath was longer. This proved that the main loss occurs due to conduction with the air surrounding the setup. Heat insulation was placed around the hot tubing to attempt to combat this loss but this also showed very little impact. Additional and better insulation on all tubing, the cells, and the HE itself could improve the heat retention but was not implemented in the current setup.

It was also observed that between the in- and outflow of the hot cell a large amount of heat is lost. While initially it could be expected due to the cell material heating up, it still lost a large amount of heat at thermal equilibrium. Some heat is converted to electricity(assumed to be equal to the P_{max}) but this would only account for a small part of the removed heat. Due to the large surface area the cell loses a large amount of heat to the air even though it is made from a poor thermal conductor(PTFE). This means to achieve a better heat retention the cell will have to be insulated as a high temperature loss is adverse to a high efficiency. Also significant amount of heat are lost between the heat bath and hot cell(+/- 5°C) so better insulation is required to retain the heat.

This brings us to determining the efficiency of the heat exchanger and the accuracy of its calculations. While we do not have temperature data from directly at the entrances and exits of the heat exchanger we do have some in close proximity. Figure 5.7 is a representation of the design and the values that were measured at the in- and outlets. For the cold side we have a temperature of approximately 20°C for both the outgoing and incoming stream. We know this from the thermocouples at the cold cell as they have temperatures approximately equal to the ambient temperature. For the hot outgoing temperature we can use the temperature recorded at the inlet to the heat bath. It was measured to be 36.3°C. For the incoming temperature of the hot side we can use the temperature recorded at the outlet of the cell which was 55.4°C. This means that over the length of the exchanger the temperature has risen by 16.5°C with a temperature approach of 19°C at the hot side. These numbers are quite far from the values of the calculation for the sizing of the heat exchanger which can be found in appendix F. Its efficiency is also somewhat lacking as based on these values it only has an heat exchange efficiency of 46.3% whereas the desired value was 83.3%. While the obtained efficiency was lower than desired it is not very low. Lee et al.[39] assumed an efficiency of 50% but they did not have many heat losses within their system resulting in a much higher heat to power efficiency. However it does show that the main problem for the heat retention is not the heat exchanger but losses to the air at the cell and from the tubing.

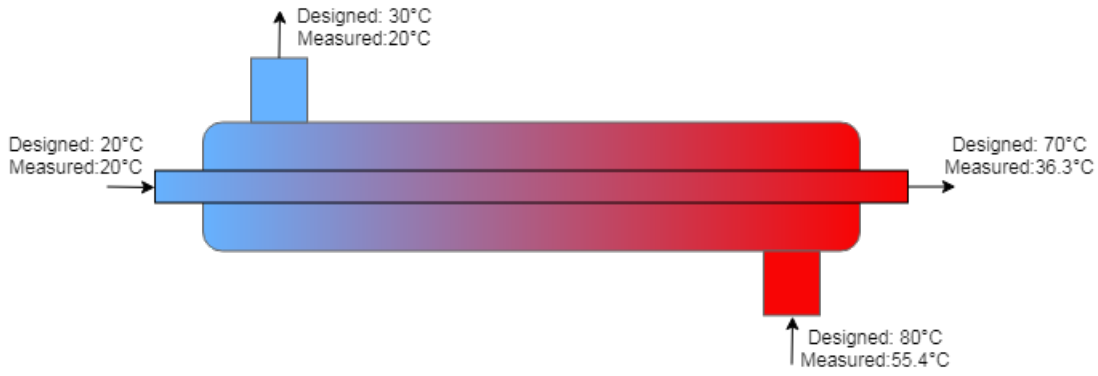

Figure 5.7: A visual representation of the heat exchanger. It shows both the designed values and the measured values for the in- and outlets. While the cold side approach the desired temperatures the hot side of the heat exchanger was far from them.

6

Chemical analysis

This chapter will contain the results of chemical analysis and determination of various errors within the project. Using various analysis techniques an attempt was made to determine changes in concentration.

6.1. Concentration analysis

The concentration of the active species has been shown to be important for the performance of the flow cell. Due to crossover of species through the membrane, the active species concentration will decrease over time. Additionally, side reactions resulting in precipitation and an imbalance of these species can influence the concentrations. Therefore it is necessary to assess the extent of the concentration change as well as the crossover. While both phenomena have similar end results, preventing them will require different strategies.

6.1.1. Ferro/ferricyanide concentration

During experiments it was noticed that ferri/ferrocyanide solution discoloured from a light green/yellow to a dark green. On the other hand the tubing which contained the iodine solution was coloured blue over time. This led to the conclusion that at least some concentration changes had to have happened as well as crossover of ionic species over the membrane. To evaluate the extent of this concentration change, a titration method was developed for both the iron cyanide solution and the iodine solution.

The iron titration was based off the standard titration of Fe^{2+} with permanganate. For this redox reaction to occur the titration had to be done in a strongly acidic medium as otherwise the permanganate would form manganese oxide which would precipitate instead of the manganese(II) ion which would be slightly pink as well as the manganese oxide reaction having a different reaction mechanism and thus a quantitative titration would not be possible. Unfortunately ferri/ferrocyanide decomposes in strongly acidic media, which, along with releasing toxic hydrogen cyanide, could change the iron composition of the solution. However due to the well established chemistry of the permanganate reaction, this was the preferred reaction to be used.

$$Fe(CN)_6^{4-} + 3H_2SO_4 \rightarrow Fe^{2+} + 3SO_4^{2-} + 6HCN \tag{6.1}$$

$$5Fe^{2+} + MnO_4^- + 8H^+ \rightarrow 5Fe^{3+} + Mn^{2+} + 4H_2O \tag{6.2}$$

Using the method described in section 3.4 the ferri/ferrocyanide solution was diluted and treated with diluted sulfuric acid. During this treatment the pH of the solution was gradually lowered and was accompanied with a colour change from a dark green to a bright green solution which can be seen in figure 6.1.This bright green is an indication of successfully stripping of the cyanide ions as iron(II)sulfate solutions have a green colour. Once this solution was made, diluted potassium permanganate was slowly added until a strong colour change was observed. However during the testing it became apparent that this colour change was very subtle. This change in colour can be seen in figure 6.1 where the colour changes to a bright red (a mixture of yellow and purple) with increasing amounts of permanganate. To determine the exact end point a titration with known values was performed, which was then used to compare colours and find the appropriate end point of the other titrations. Equations 6.1 and 6.2 give the reaction equations that are involved with the titrations.

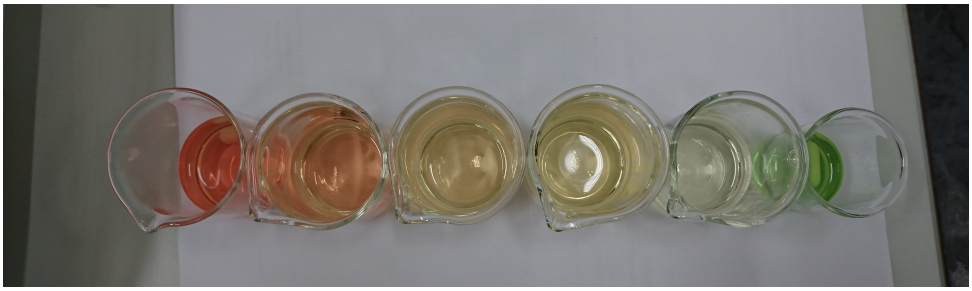

Figure 6.1: A picture of the titration of the iron solution at various stages. The amount of titrant decreases from left to right and as can be seen the colour of the solution slowly turns more yellow. The fourth beaker shows the desired colour and the point at which the reaction has been determined to be finished. The beaker at the far right shows the solution after adding the acid. This bright green is associated with iron(II)sulphate and this is also the reason why the green fades after adding titrant as the iron(II) is converted.

Figure 6.2 shows the results of both the titrations and the absorption measurements over time for the ferrocyanide species. Except for the third measurement the concentration seems to follow an asymptotic line where the concentration drops by about 0.25 M over the given time period. This is approximately 16% of the total concentration. This degradation is agreements with similar values found in literature on the degradation of the ferrocyanide species.[56] It is also seen that the very first sample which was taken before being in contact with the iodine solution has also decreased significantly. It has lost about 8% of its original concentration which can all be attributed to the degradation caused by light. Also interesting is the third sample which has a much lower concentration and therefore seemed like an outlier. However after performing the absorption measurements it seems to be accurate as they produced approximately the same concentration for the third for the ferrocyanide species. Appendix E shows the exact values for all the performed titrations.

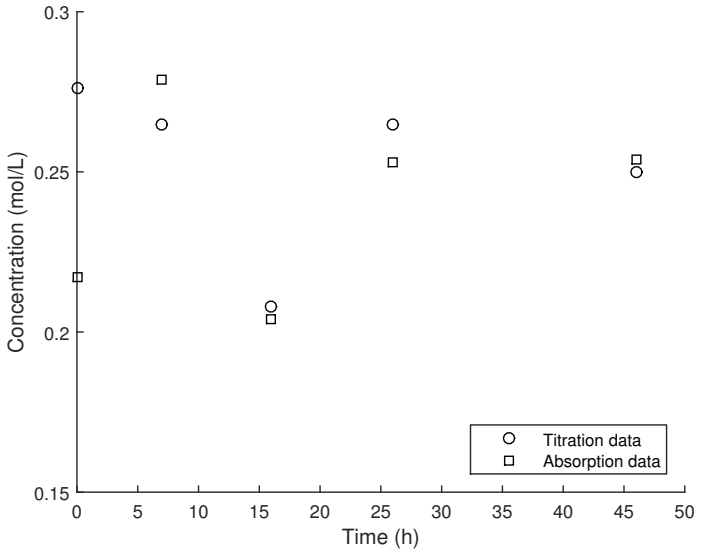

Figure 6.2: A graph showing the change in concentration over time for the ferrocyanide species. Aside from the first measurements the measured values for both methods are close. It also shows that the concentration gradually decreases over time with a strange outlier for the third measurement.

UV-VIS absorption measurements were performed to gauge the accuracy of the titration method for the ferrocyanide as well as to assess the concentration of all the other species. As can be seen in figure 6.2 the obtained concentration values are in somewhat good agreement except for the first sample. In particular the third sample is interesting as even though the concentration is much lower than the other samples the obtained values nearly match. The values for the other species can be found in table E.4. It shows that there was no iodide and only a small amount of triiodide present in the sample which was unexpected. It is not possible for triiodide to exist in the ferro/ferricyanide solution as it will spontaneously react with the ferrocyanide species. This table also shows a very large increase in concentration for the ferricyanide species. This

increase is impossible as the it is much larger than the initial concentration and the change cannot be supplied by converted ferrocyanide as its concentration has not dropped enough. Figure 6.3a shows how well the fit for the model is for the ferro/ferricyanide sample. Therefore the observed errors are likely a result of incorrect dilution and dissolution. To increase the accuracy of both methods a larger range of samples needs to be tested to confirm their accuracy. In particular the absorption measurements can be improved by measuring for a larger range of wavelengths which will allow the iodide species to be detected.

Finally ICP-MS measurements were performed to confirm the extent of the concentration drop. As be seen from table E.6 the iron concentration has definitely dropped as the expected value is approximately 33.5 g/L. Contrary to the values obtained for the other measurement techniques, the ICP-MS showed that the iron concentration is almost the same for all the samples. This would indicate that degradation (Prussian blue formation and cyanide ligand loss) is the main cause of a decrease in concentration as it would happen at the same rate for all samples. It also shows that the absolute iron concentration values obtained by the absorption are somewhat off. However that would contradict some of the titrations and therefore it is highly possible that only the ferricyanide reference is incorrect as it is the main cause of the high total concentration. All the results combined do point to an imbalance in the concentration of the active species possibly due to different rates of degradation or unequal conversion at the electrodes. The ICP-MS also show a strong increase in potassium as the expected value is 80 g/L while 88 g/L was measured. The only possibility for this variation is the crossover from the iodide/triiodide solution which seem to be supported by the values measured for the iodide samples.

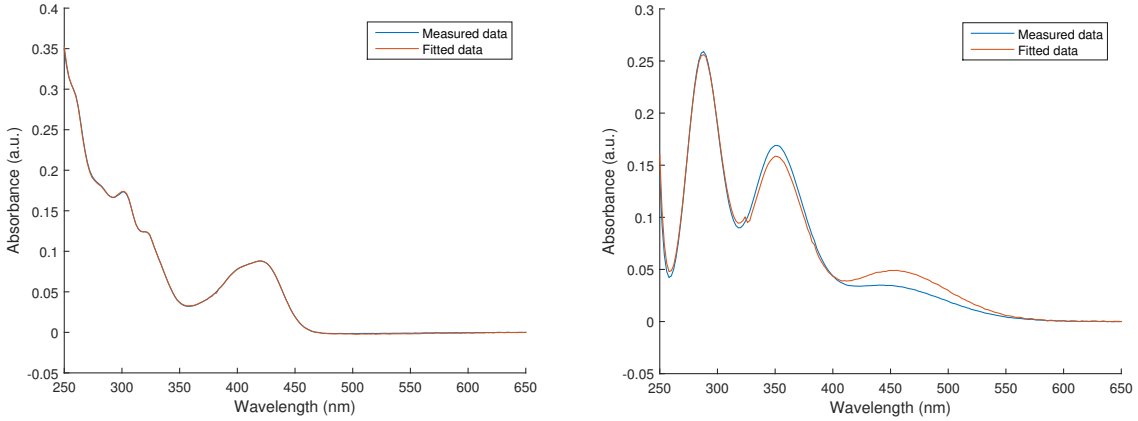

(a) $Fe(CN)_6^{3-}/Fe(CN)_6^{4-}$ solution measurement

(b) I_3^-/I^- solution measurement

Figure 6.3: (a) A plot showing the measured absorption spectrum and the fitted spectrum for the ferro/ferricyanide solution. As can be seen the fitted comes very close the the measured spectrum which was true for all measurements with the worst fit having r^2=0.999. (b) A plot showing the measured absorption spectrum and the fitted spectrum for the iodide/triiodide solution. It shows the general curve for all the measurements having an approximate r^2=0.9786. The fit for these measurements is slightly worse than the ferro/ferricyanide measurements. In particular the area between 400-500 nm shows an improper fit.

6.1.2. Iodide/triiodide concentration

To determine the iodide/triiodide concentration, a suitable redox couple had to be established in a similar fashion as for the ferri/ferrocyanide reaction. At first a similar permanganate solution seemed like a viable titrant but due to triiodide solution having a dark brown colour this was useless as there was no defined colour transition. Therefore the triiodide had to be converted as an iodide solution would be colourless. Thus permanganate was excluded as a possible titrant. A new titrant had to be found and while looking at a list of standard potentials, it was noticed that ferrocyanide could be used as a titrant. The knowledge that this reaction could work also resulted in the conclusion that there would only be iodide ions present in the ferri/ferrocyanide solution. During this reaction the dark brown colour should disappear and be replaced by the yellowish colour of ferricyanide. This titration does not have the problem of gradual colour change as the triiodide ion is such a strong colourant that even at very low concentration its brown colour is still visible. Therefore the endpoint could be seen somewhat easily. Equation 6.3 shows that reaction that occurs during the titration.

$$I_3^- + 2Fe(CN)_6^{4-} \rightarrow 3I^- + 2Fe(CN)_6^{3-} \tag{6.3}$$

Figure 6.4 shows the results of both the titrations and the absorption measurements for the triiodide species. As can be seen for the titration the triiodide concentration does not vary much is is approximately 0.25 M for all samples. This indicates that the concentration has dropped by a similar percentage as the ferrocyanide species however other factors have indicated that is not due to to crossover. The change in concentration is most likely caused by the evaporation of elemental iodine due to the equilibrium reaction as well as triiodide leaching into the storage tubes as can be seen in figure D.4. This brings up a similar problem as for the ferrocyanide measurements as the sample will have lost some triiodide to the test tubes and therefore does not accurately reflect the concentration of the sample when it was taken.

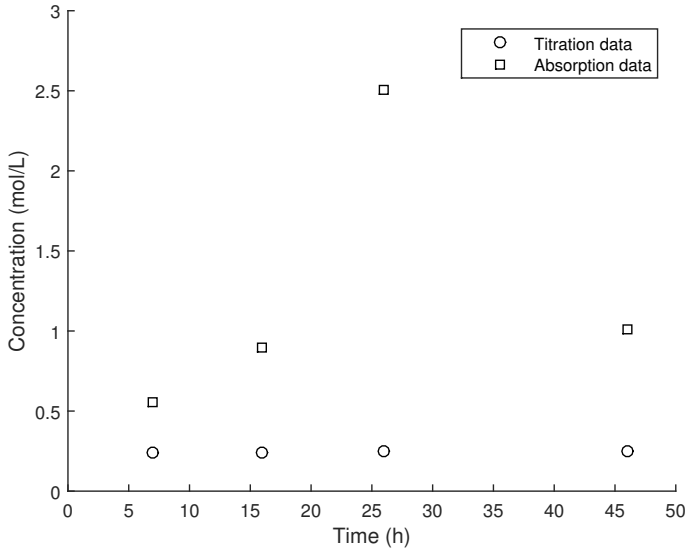

Figure 6.4: A graph showing the change in concentration over time for the triiodide species. As can be seen the concentration obtained from the titrations is relatively constant over time whereas the results from the absorption fluctuate a lot and are much too high.

The triiodide concentration was also investigated using UV-VIS absorption. Using the same model from section 6.1.1, the acquired measurements could be fitted. Figure 6.4 also shows the concentration that was obtained from the absorption measurements. As can be seen the values vary wildly over the samples with most concentrations being very unlikely. Again this could be caused by the reference being improperly prepared but due to the large variations it seems that something else is at play. Especially when compared to the titrations and absorption measurement for the ferro/ferricyanide samples which all result in somewhat plausible concentrations this seems to be the case. Another possibility is the non-linear increase in absorption with concentration, which while unlikely was observed by Kireev et al.[57] for the triiodide species. Furthermore figure 6.3b show the accuracy of the average fit for the triiodide samples and it seems to indicate that another component is present in the solution due to somewhat strong absorption in the 400-500 nm range. This could be another polyiodide species or some iron-containing compound that forms as a result of the crossover of ferro/ferricyanide (very likely Prussian blue (Ferric ferrocyanide) which absorbs in approximately these wavelengths).

The concentrations of the other species can be found in table E.5. As can be seen no ferro/ferricyanide was present which would be expected as the iodide solution is slightly acidic and thus the cyanide ions would be removed from any ions that crossed over. Additionally the ferro/ferricyanide tended to precipitate in this solution which would also result in no ions being present. Also no iodide was measured which is due to the minimal absorption in the investigated wavelength range which means the script cannot assign any values to its concentration.

As the ferro/ferricyanide crossover could not be determined by titration or UV-VIS absorption of the iodine samples, a different analysis method had to be used. ICP-MS could perform this analysis and thus give conclusive results of crossover. Table E.7 shows the results of this analysis. It shows that there is indeed a crossover of iron atoms. There are two causes for the minimal concentration change over time, namely either

iron crossed over and precipitated(visible by the turning blue of the tubing) or an equilibrium is established over the membrane. An anomaly in the measurements is that the potassium concentrations are lower than they should be. Even for the fresh samples, it is 5 to 7 g/L lower than it should be. As stated earlier a part of this is caused by diffusion into the plastic of the sample test tubes but due to the potassium concentration of the ferro/ferricyanide samples being higher it is also likely that a large amount crossed over. To confirm this further measurements are required which can measure both the iodide and triiodide concentration in all samples.

6.2. X-ray Photoelectron spectroscopy (XPS)

As mentioned in section 3.1, over time the graphite electrodes exhibited leakage as a result of their porosity. Therefore titanium electrodes were made to replace them. Titanium should be chemically resistant and provide enough conductivity and surface area to allow for the electrochemical reactions to occur. However, this would come with a penalty of a higher resistance as from literature[18,37] it is known that carbon materials are among the best for these reactions. To assess the viability they were tested outside of the flow cell. First this electrode was tested in a solution containing only the ferri/ferrocyanide couple. Immediately when the experiment started very large overpotentials were visible and once it had concluded, the titanium had changed colour which can be seen in figure 6.5. The gold-brown coloured part had been immersed in the solution whereas the silver coloured part had remained above the liquid level. This gold-brown colour was assumed to be iron oxide and to confirm this assumption XPS measurements were performed. The electrode in figure 6.5 also shows small brown deposits which were also assumed to be iron oxide.

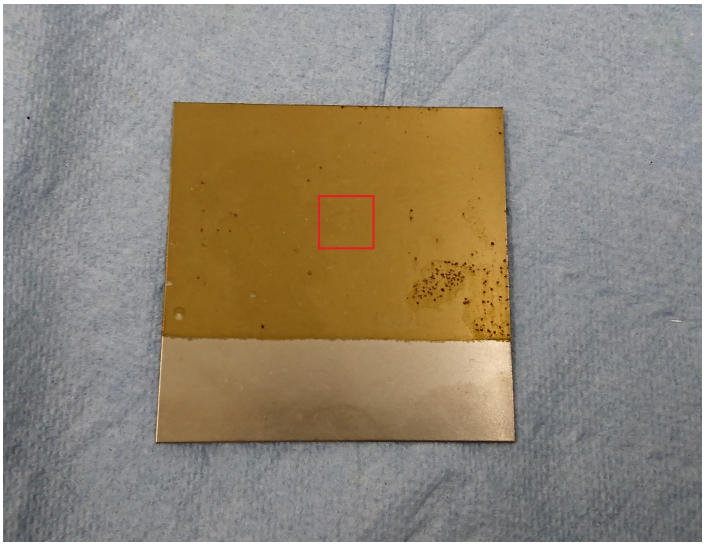

Figure 6.5: A picture of the electrode after being used in the ferro/ferricyanide solution. the silver at the bottom is the original colour of electrode whereas the gold/brown has been in contact with the solution. The red box is the approximate location of the XPS measurement. The brown agglomerates present at the bottom right are probably iron(III) oxide.

The figures at the end of appendix E show the results of this XPS measurement. The measurement point was chosen to be in the center of the electrode and does not take into account the brown deposits. As can be seen from figure E only minute traces of iron are present which are barely visible above the background noise signal. With the given elements available in solution the peaks were assigned which indicated that the main compound present was titanium dioxide. However this would not explain the brown colour as TiO_2 is a white compound. The measurement also reported that a large amount of carbon was present along with a small amount of nitrogen. This carbon presence could be explained by carbon dioxide adsorbed onto the surface but the presence of nitrogen could not be explained in the same way. Using a database the peaks were assigned once more which indicated the the compound titanium nitride (TiN) was present in the sample.

After doing research on the Internet this indication was confirmed as TiN does have the gold-brown colour that was seen in the sample(It is used as a coating for drill bits). This is quite remarkable as the same research showed no results for electrochemical production of titanium nitride. The formation of titanium nitride could explain the unusually high overpotential as it would require the electrochemical decomposition of the cyanide ion. While unintended, this measurement might open up a route to the electrochemical forma-

tion of titanium nitride. These experiments have confirmed that titanium would not be a suitable electrode as the required redox reaction does not occur. Additionally, both titanium dioxide and titanium nitride have somewhat poor conductivity compared to graphite and pure titanium. Therefore any further investigation of this reaction and electrode composition was ceased as it would deviate too far from the original research.

6.3. Removal and recuperation of crossover

As stated in section 6.1, crossover of ionic species occurs through the membrane. While it might not have a direct or significant influence on the performance of the flow cell, over time it will cause a lowering of concentrations as well as depletion of particular ionic species. Therefore it is critical that these impurities can be removed and preferably can be reintroduced into the original solution to reduce the costs of replenishing or replacing the solutions. There are many options for removing ionic species like precipitation, ion exchange, eutectic freezing and other crystallization methods. However many of these methods are quite energy and resource intensive and are therefore unsuitable for this setup as they would drastically decrease energy efficiency.

Firstly the iodine solution was investigated. From the discolouration of the tubing and spacer it was evident that some ferri/ferrocyanide had crossed over into this solution. This observation was supported by ICP-MS measurements which also indicated crossover of the iron atoms. While it is undesired that this compound deposits inside the setup, it does give a potential method of removal. By adding iron chloride, a precipitate of Prussian blue should form while only potassium chloride remains. This does mean that with subsequent ferri/ferrocyanide removals the potassium chloride concentration will increase until it reaches saturation. Additionally, the amount of iron to be added would need to be carefully calculated in order to not add an excess which would defeat the purpose of the initial removal.

Secondly the ferri/ferrocyanide solution was investigated. It had already become apparent that some iodide and triiodide had crossed over to this solution and that all the triiodide had reacted to iodide. This made the separation particularly difficult as iodide is hard to remove. Triiodide could have been removed easily, as it forms a complex with starch which can be filtered out of the solution. This is not the case for iodide. It can be removed through precipitation or using very advanced membranes. For a precipitation of iodide, a silver compound could be added, but this would result in an unwanted anion entering the solution. Additionally, silver ions react with the ferro/ferricyanide and thus the entire attempt would not work. This means that only a membrane method would remain. However this membrane will very likely also transport chloride which is unwanted as well as the high cost such a specialized membrane will have. Therefore the best option will be to just replace the liquids when necessary. It has not yet been established what the full extent of the crossover is and how much it interferes with the operation of the setup. To be able to ascertain the concentration at which replacement is required, more stability measurements will have to be performed over a long time period.

Another difficulty is the degradation of ferri/ferrocyanide due to being exposed to light. As is evident from results presented in section 6.1.1, the largest decrease in concentration is not the result of ionic crossover but from degradation of the active components. Based on literature this internal degradation would be a relatively easy phenomenon to prevent as by storing the solution in dark glass bottles the apparent degradation did not occur as rapidly.[56,58] Moreover, all the tubing used in this experiment could be encased in insulation material which would decrease the exposure to light so the solution would permanently be in the dark. While this will reduce the rate of degradation, the degradation is inevitable and irreversible so at some point new electrolyte will be required. Again more and longer stability measurements are required to be able to assess the true extent of the degradation and the time after which the electrolytes need to be refreshed.

7

Conclusion

In this thesis the validation, optimization and analysis of a thermo-electrochemical flow cell was performed. This was done by circulating liquids between a hot and a cold cell where one half cell of each contained the $Fe(CN)_6^{3-}/Fe(CN)_6^{4-}$ redox couple and the other half cell contained the I_3^-/I^- couple.

During the validation and optimization phase the various results obtained by my predecessor were recreated. Furthermore some predictions made by him were confirmed. During the optimization various properties were assessed for their impact on the resistance of the cell. The setup design and properties were changed in such a way that the resistance at the end was almost 7 times lower than at the very beginning of the project (6.73 Ωcm^2 vs. 42.9 Ωcm^2). This decrease was realized by changing the electrolyte concentrations, the flow rate and the thickness of the cell. These changes also increased the Seebeck coefficient to -2.88 mV K^{-1} which is very high for only aqueous electrolytes. Thus in theory we could calculate that the setup would have a normalized maximal power output of 2.40 $mWm^{-2}K^{-2}$ (75 mW output for the theoretical system) and an absolute efficiency of 0.09% (relative efficiency of 0.53%). These power output results would be phenomenal and easily surpasses all previous work.

Once all the optimal conditions were established, the setup was completed with the integration of heat exchangers. Then the entire setup was assessed for its power output and efficiency. While falling below expectations at a normalized maximal power output of 0.33 $mWm^{-2}K^{-2}$ (5.15 mW output for the current system) and an absolute efficiency of 0.004% (relative efficiency of 0.03%), it performs similar to other thermo-electrochemical cells. The low power output was the result of an increased resistance and lowered Seebeck coefficient(-2.02 mV K^{-1}) compared to the optimal values. Additionally the custom designed heat exchanger was tested and compared to its design values. Its heat exchange efficiency was 46.3% compared to the expected 83.3%. This brought to light an additional problem of heat management within the entire setup as large losses were observed in all components. Aside from the heat loss there was also a performance loss as over time the results became worse due to electrolyte degradation. Thus the main drawbacks of the system were the electrolyte stability and the heat management.

To assess this loss of performance and its cause a variety of analysis techniques were applied. Using redox titration, UV-VIS absorption, and ICP-MS measurements, the changes in concentration due to degradation and crossover were assessed. It became clear that while it was initially thought that crossover played a large role in the decrease in performance it was actually the degradation of the electrolytes. The titration methods proved difficult to use accurately as often no clear endpoint could be established. Therefore they were coupled with the UV-VIS absorption. To be able to assess the concentration from the absorption a model was established. This model showed some accuracy but only to a certain degree and needs further improvement. Both of these methods could only determine the degradation and crossover combined and therefore ICP-MS was used to measure the crossover of the ferro/ferricyanide species. This showed that there was indeed crossover however it was minute compared to the degradation.

All in all the thermo-electrochemical flow cell design shows promise. While only marginal power outputs were obtained and the stability was far from desired, the characterization measurements showed great promise for high power outputs. To get a more workable setup the heat-to-power efficiency will need to be significantly increased. However with the current output it can compete with some previously established systems and with the theoretical power output it can outperform most in terms of normalized power output.

8

Recommendations

As has been demonstrated the current design functions but is far from optimal. Therefore there are a few recommendations which if implemented properly could bring the design to a higher level and possibly outperform all other currently available research.

Firstly, the setup should be improved to reach the theoretical limit that was established which means a higher Seebeck coefficient and a lower resistance need to be achieved. To improve the Seebeck coefficient more information on it needs to become available. Further research into the fundamental behaviour is needed to be able to predict the behaviour. Additionally the effect of solvents can be assessed as it has been shown that they can increase the Seebeck coefficient. As for the resistance, the exact source of the extra resistance in the full setup needs to be identified by measuring each component independently. While it could be a result of decreased concentrations, it has been shown that poor electrical contact in the wiring could also be cause given the small resistances that are dealt with.

Secondly, the heat management needs to be improved. As mentioned before extra insulation should help protect against the heat loss over the tubing but a solution also needs to be found for the cells themselves as this is where the largest loss of heat is incurred. This could be done by insulation as well but possibly there are better alternatives. Furthermore the heat exchangers need to be improved as currently they are not being used to their full potential. The design could also be rigorously changed by only heating the electrodes as it was determined that the main loss of efficiency comes from the incredible amount of heat that is required (compared to the produced power) to heat liquids. Possibly this can be optimized thereby reducing the heat requirements.

Thirdly, the electrolytes need to be assessed. While they have shown the ability to achieve high Seebeck coefficients, they also have their downsides. The main issue for the ferro/ferricyanide was the stability of the solution and therefore a method needs to be developed to increase the stability as it currently hampers the quality and reproducibility of the results. Coupled with this the analysis techniques need to be improved as currently their accuracy is questionable. The main issue with the iodide/triiodide solution is the corrosivity of the solution. While it was not such a big problem for the current thesis (although restrictive in the usable materials), it could have much larger effects in the long term operation. Therefore other electrolytes need to be investigated to find the trade-off between the stability and the performance.

Finally, the cell itself can be improved. As has been discussed the electrodes are not stable enough and require replacement. A smaller cell would also be beneficial as it would made the entire setup smaller and therefore less resource intensive as well as making the heat management easier as there will be less distance to transport it over. All in all quite some improvements are necessary to make this setup perform at its best.

A

Derivations of used equations

In this appendix various derivations and formula's will be discussed and explained/expanded.

Below is the derivation for the Seebeck coefficient:

Starting with the general equation for the Gibbs energy,

$$\Delta G = \Delta H - T\Delta S \tag{A.1}$$

we can substitute the ΔG for the equation for the Gibbs energy given in section 2.1, which results in the following equation:

$$E = \frac{T\Delta S - \Delta H}{nF} \tag{A.2}$$

Then the derivative to temperature has to be taken in order to get a value of volt per kelvin. This operation results in the following equation:

$$\alpha = \left(\frac{dE}{dT}\right) = \frac{\Delta S}{nF} + \left(\frac{T\left(\frac{d\Delta S}{dT}\right) - \left(\frac{d\Delta H}{dT}\right)}{nF}\right) \tag{A.3}$$

It can be assumed that both ΔS and ΔH are independent of temperature(due to the minimal variations with temperature) which means that the second term can be dropped from the equation which results in the final and generally accepted formula:

$$\alpha = \frac{\Delta S}{nF} \tag{A.4}$$

To calculate the power efficiency we start with the Carnot efficiency:

$$\eta_{Carnot} = 1 - \frac{T_c}{T_h} \tag{A.5}$$

The energy efficiency is determined by various sources of gains in energy divided by losses and inputs of energy such as the electrical losses, heat input and pumping power which results in the equation seen in section 2.2:

$$\eta_{absolute} = \frac{\alpha \Delta T I - (R_{Charge} + R_{Discharge}) I^2}{\dot{m} * C_p \Delta T + \frac{8\mu l Q^2}{\pi r^4} * 2} \tag{A.6}$$

Then the relative efficiency can be determined by dividing by the Carnot efficiency:

$$\eta_{relative} = \frac{\eta_{absolute}}{\eta_{Carnot}} * 100\% \tag{A.7}$$

To calculate the maximum power output of the current design we start with the general equation for power:

$$P = UI \tag{A.8}$$

where we substitute the potential for the various potentials and losses with in the cell:

$$P = (U_{Charge} - IR_{Charge} - U_{Discharge} - IR_{Discharge})I = \alpha \Delta T I - (R_{Charge} + R_{Discharge})I^2 \tag{A.9}$$

To get the maximum power the equation will have to be differentiated with respect to I which results in:

$$I(\frac{dP}{dI} = 0) = \frac{\alpha \Delta T}{2(R_{Charge} + R_{Discharge})} \tag{A.10}$$

Substituting this value for I back in the original equation yields the equation for the maximum power:

$$P_{max} = \frac{(\alpha \Delta T)^2}{4(R_{Charge} + R_{Discharge})} \tag{A.11}$$

The equation to describe the pressure drop over the cell is as follows:

$$\Delta P = 2.107 \frac{N_f}{A} \sqrt{r^3 u_x^3 sin^3(\theta/2) \rho \mu} + 0.5 N_f \frac{A_p}{A} \rho u_x^2 sin^2(\theta/2) + 0.5 \rho N_t k_\theta \frac{A_\theta}{A} \frac{u_x}{cos(\theta/2)} + \frac{12 u_x \mu L \epsilon}{h^2} \tag{A.12}$$

where the following values are used for the various parameters:

Table A.1: A table containing the various parameters that were used to calculate the pressure drop within the cells.

Parameters

Definition	**Unit**	**Value**	**Definition**	**Unit**	**Value**
Filament radius (r)	m	$1.08 * 10^{-4}$	Drag coefficient (C_d)	-	38.3
Axial velocity (u_x)	m/s	0.03	Friction loss factor (k_θ)	-	50
Density (ρ)	kg/m^{-3}	1000	Spacer height (h)	m	$3.85 * 10^{-4}$
Dynamic viscosity (μ)	Pa*s	$1.08 * 10^{-3}$	Hydraulic diameter (d_h)	m	$6.5 * 10^{-5}$
Filament angle (θ)	Deg	90	Specific spacer surface (S_{Vap})	m^{-1}	18604
Channel length (L)	m	0.3	Spacer voidage (ϵ)	-	0.29
Channel height (h)	m	$4 * 10^{-4}$	Channel width (w)	m	0.03
Channel surface (A)	m^2	$1.2 * 10^{-5}$	Filament diameter	m	$2.2 * 10^{-4}$
Frontal projection surface (A_p)	m^2	$6.5 * 10^{-8}$	Mesh size (l_m)	m	$3 * 10^{-4}$
Cross-sectional mesh area (A_θ)	m^2	$5.8 * 10^{-8}$	Number of filament (N_f)	-	1109
Reynolds number (Re)	-	1.7	Number of flow changes (N_t)	-	1108

The equation for the various parameters can be found in the work done by Da Costa et al.[49] k_θ was approximated by taking the value for the lowest available Reynolds number. The drag coefficient was calculated with 64/Re as the Reynolds number was very low (1.7).

B

Chemicals and equipment

This appendix chapter will detail all the various chemicals used for this thesis as well as all the equipment.
Below the list of chemicals:

- Potassium hexacyanoferrate(III), $K_3Fe(CN)_6$, >99%, Alfa Aesar/Roth
- Potassium hexacyanoferrate(II), $K_4Fe(CN)_6 * H_2O$, >99%, Alfa Aesar/Roth
- Iodine, I_2, >99%, Alfa Aesar
- Potassium iodide, KI, 99%, Alfa Aesar
- Potassium chloride, KCl, >99%, Merck KGaA
- Potassium permanganate, $KMnO_4$, >99%, Alfa Aesar
- Sulfuric acid, H_2SO_4, 6.0N standardized, Alfa Aesar

The list of materials and equipment:

- Flow Cell
  - Flow cell, DEMO TU Delft, Custom design using Autodesk Creator
  - Gaskets, Eriks, FPM/FKM rubber
  - Membrane, Selemion, CMV cation exchange membrane
  - Spacer
    - 3D printed spacer, Oceanz 3D printing, PA2200 custom design
    - Flow spacer, SEFAR, Fluortex 09-300/36
  - Electrodes
    - Graphite sheet, Alfa Aesar, 0.4 mm
    - Titanium, Titaantrade, Grade 1 0.4mm
  - Wiring
- Pump, Masterflex, Precision peristaltic pump EW-07528-10 with pumphead 77202-60
- Potentiostat, Ivium, Vertex & Iviumstat
- Temperature sensor
  - Thermocouples, TC Direct, 405-011 K-type thermocouple
  - Temperature input module, National Instruments, NI 9213
- Heat exchanger, Squall Instruments, Custom design 1m length and 70 double coils

- Heat bath, Julabo, Corio C-B19
- Cold bath, Julabo, Corio CD-601F
- PTFE tubing, Ebora, 6/8mm tubing
- Tubing connectors, Em-Technik, 1A100T43PP & 1A100T4340PP & 1A100MN4312PP

List of used computer programs:

- Ivium
- Labview
- Matlab
- Excel
- OLI Studio

C

PFD flow cell

Table C.1: A table containing the equipment numbers and what they represent for both the pfd's.

Single cell setup		Full setup	
Equipment number(E-x)	Equipment	Equipment number(E-x)	Equipment
1	Pump	1	Heat exchanger
2	Storage vessel	2	Pump
3	Storage vessel	3	Heat exchanger
4	Heating bath	4	Storage vessel
5	Heating bath	5	Storage vessel
6	Flow cell	6	Heating bath
7	Potentiostat	7	Heating bath
		8	Hot flow cell
		9	Cold flow cell
		10	Cooling bath
		11	Cooling bath
		12	Potentiostat

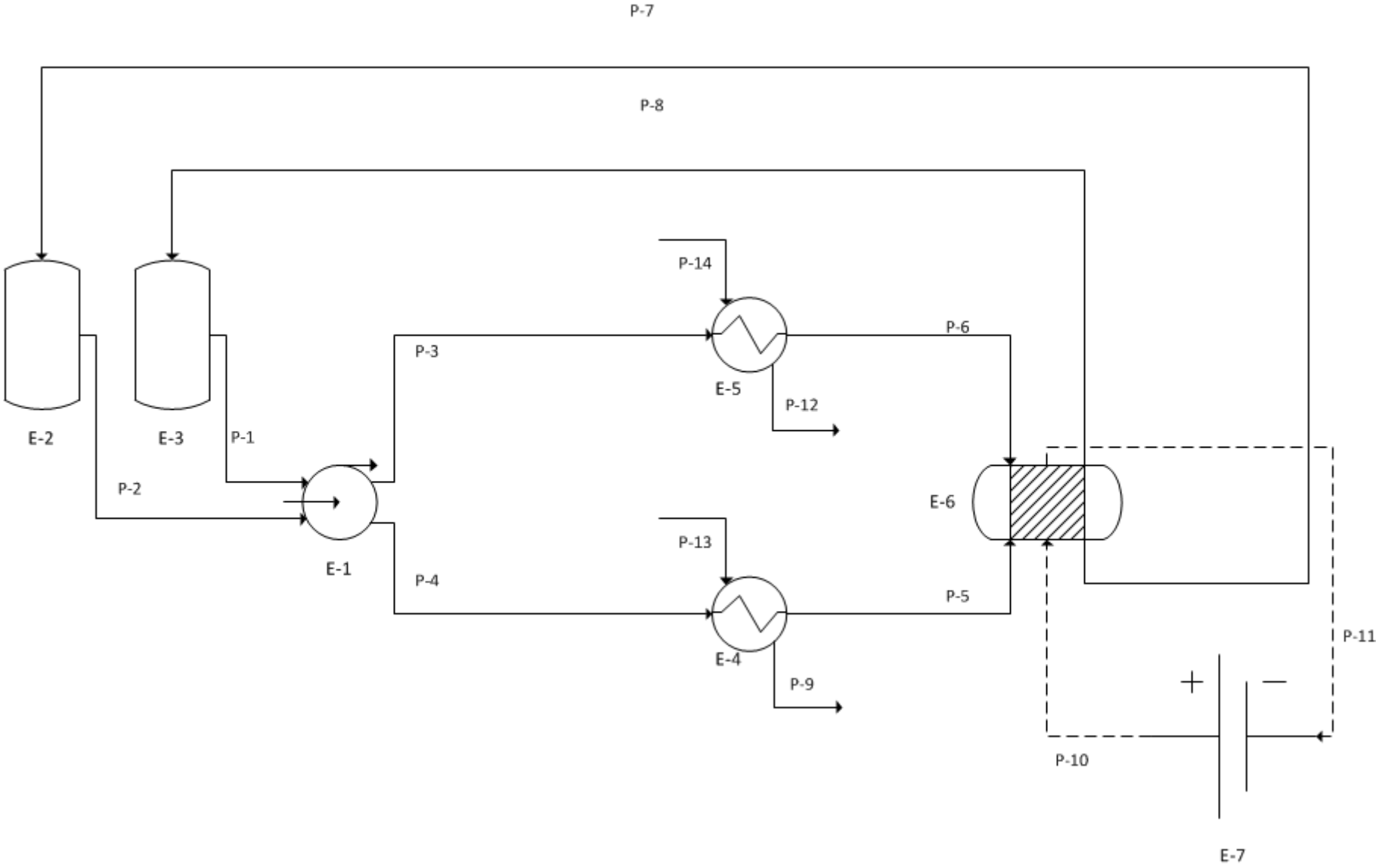

Figure C.1: A flow diagram giving a schematic overview of the cell setup for characterization with a single cell.

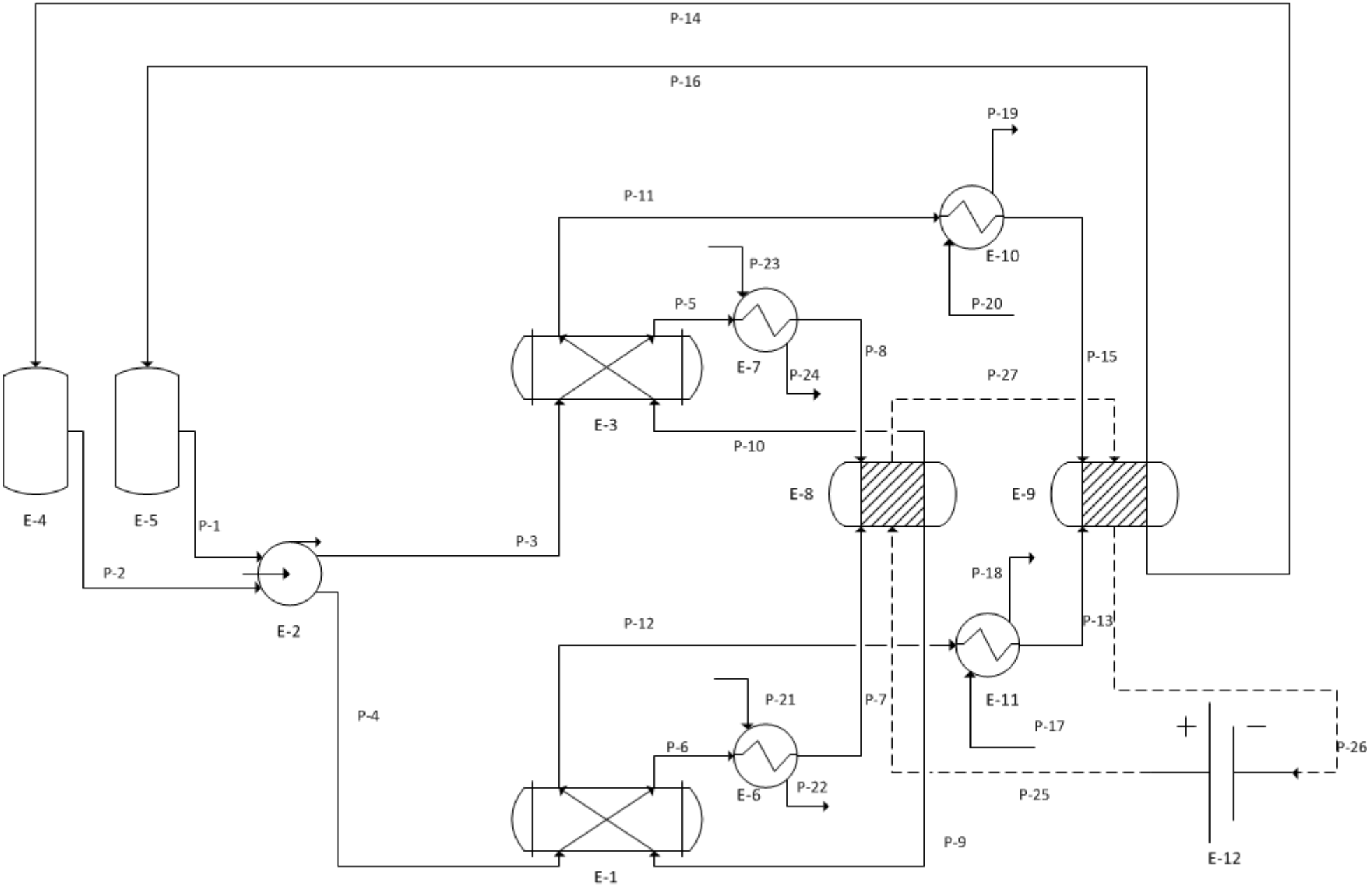

Figure C.2: A flow diagram giving a schematic overview of the cell setup for assessment of the power output and the efficiency.

D

Pictures of setup and damage

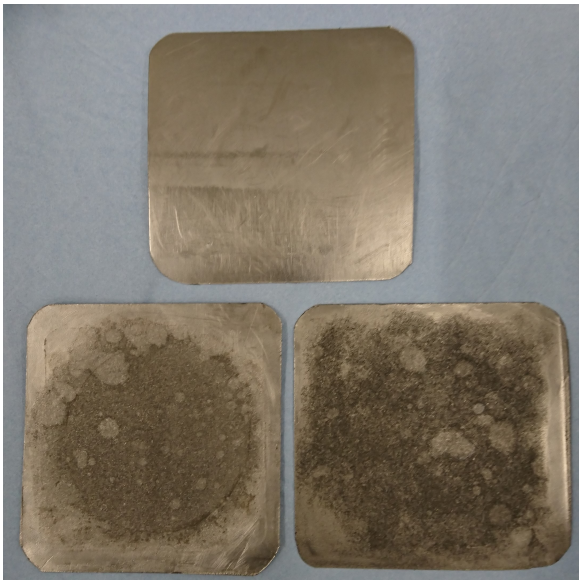

Figure D.1: A picture showing the damaged electrodes. At the top a fresh electrode. The bottom left electrode has been in contact with the ferro/ferricyanide solution. The bottom right electrode has been in contact with the iodine solution.

Figure D.2: A picture showing the fouling/damage of the membrane with the brown/black being iodine related fouling and the blue fouling being Prussian blue deposition.

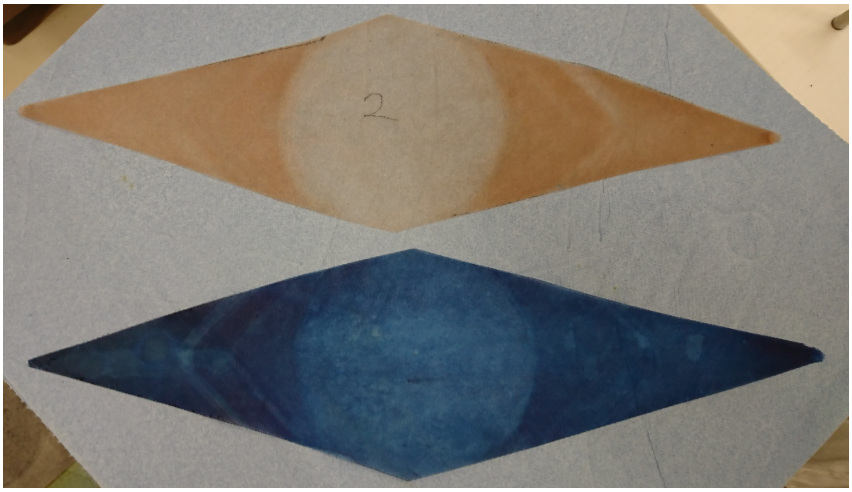

Figure D.3: A picture of the discoloured spacer mesh. The brown mesh (top) is from the ferro/ferricyanide side and is likely iron oxide deposition. The blue coloured mesh (bottom) is from the iodine side is is Prussian blue deposition.

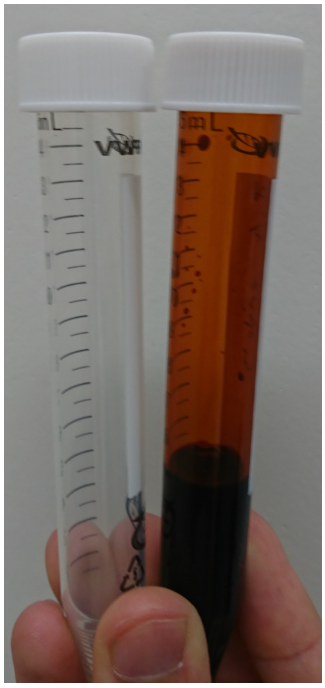

Figure D.4: A picture of the test tubes the samples were stored in. Left is a new tube and right is a tube holding an iodine sample. As can be seen the tube is strong discoloured due to the triiodide leaching into the plastic.

E

Various results and graphs

Power acquisition method

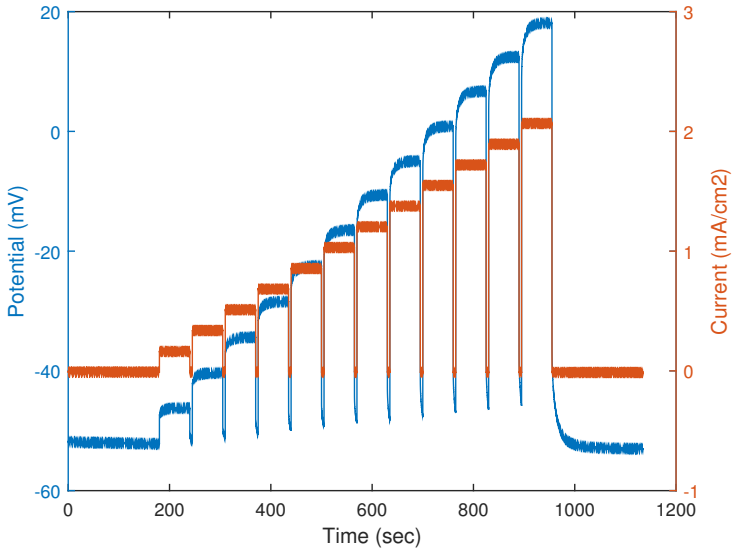

Figure E.1: An example for a measurement done for the power curve. As can be seen when the current increases the overpotential increases. Once the potential goes over 0 V no net power is produced. This measurement was performed at a temperature difference of 24.5°C.

Chemical analysis results

Table E.1: A table showing the various samples and the times at which they were taken. The sample on 29/5 was taken after filling the HE and preparing the entire setup for operation. The first sample on 30/5 was taken after completing the flow loop and letting the electrolytes run for a few minutes. The second 30/5 sample was taken after a full day of running experiments and the sample on 31/5 was taken just for later reference. The fresh samples are taken right after production of the solutions.

Ferro/ferricyanide sample		**Iodide/triiodide sample**	
Sample X	**Reference time**	**Sample X**	**Reference time**
Sample 1	Fresh	Sample 1	29/5 17:00 (After HE)
Sample 2	29/5 17:00 (After HE)	Sample 2	30/5 8:45
Sample 3	30/5 8:45	Sample 3	30/5 18:45
Sample 4	30/5 18:45	Sample 4	31/5 13:00
Sample 5	31/5 13:00	Sample 5	Fresh

Titration results

Table E.2: The results for the titration of the ferro/ferricyanide samples. The reference was made to have a molarity of 0.3.

	Measurement 1 (mL)	Measurement 2 (mL)	Average (mL)	mMol	M (mol/L)
Sample 1	8.4	8.2	8.3	0.0415	0.276667
Sample 2	8.1	7.8	7.95	0.03975	0.265
Sample 3	5.9	6.6	6.25	0.03125	0.208333
Sample 4	7.9	8	7.95	0.03975	0.265
Sample 5	7.5	7.5	7.5	0.0375	0.25
Reference	9	8.9	8.95	0.04475	0.298333

Table E.3: The results for the titration of the iodide/triiodide samples. The reference was made to have a molarity of 0.1.

	Measurement 1 (mL)	Measurement 2 (mL)	Average (mL)	mMol	M (mol/L)
Sample 1	5.1	4.5	4.8	0.144	0.24
Sample 2	4.8	4.9	4.85	0.1455	0.2425
Sample 3	5.1	4.7	4.9	0.147	0.245
Sample 4	5.1	5.0	5.05	0.1515	0.2525
Reference	2	2.1	2.05	0.0615	0.1025

Absorption results

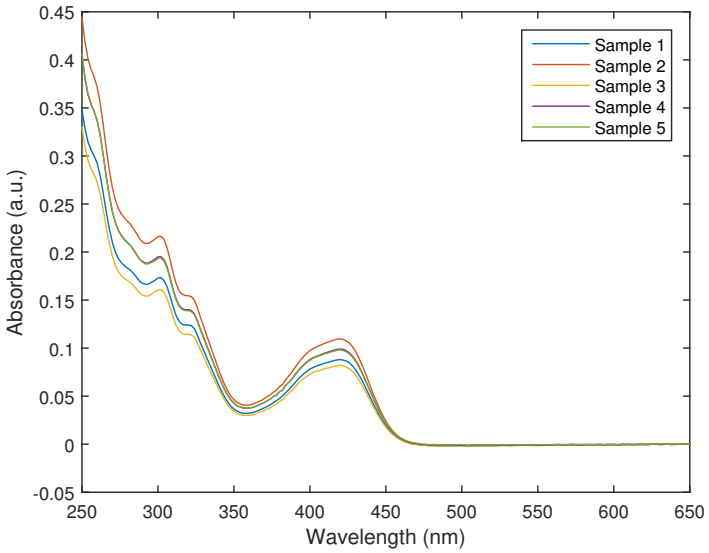

Figure E.2: A graph showing all the absorption spectra for the various ferro/ferricyanide samples.

Table E.4: The concentrations that were obtained from fitting data to the absorption spectra from figure E.2.

	$Fe(CN)_6^{3-}$ (M)	$Fe(CN)_6^{4-}$ (M)	I_3^- (M)	I^- (M)
Sample 1	0.32694	0.21687	0.00666	0
Sample 2	0.4059	0.27891	0.0096	0
Sample 3	0.30303	0.20412	0.00522	0
Sample 4	0.36558	0.25323	0.0102	0
Sample 5	0.3603	0.25473	0.01281	0

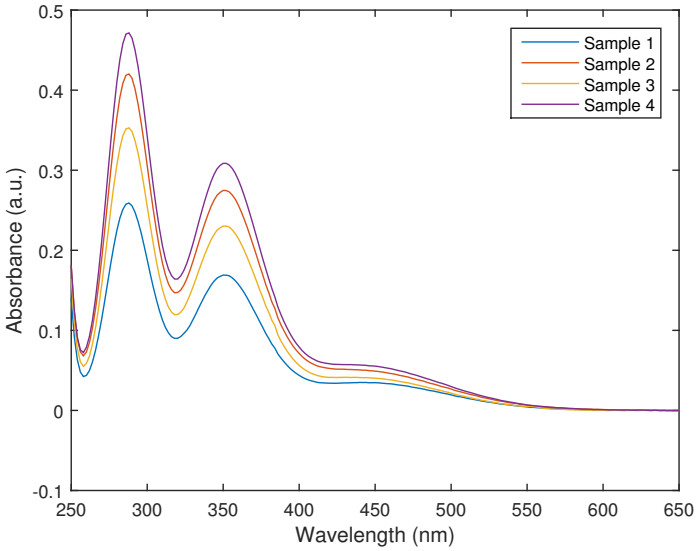

Figure E.3: A graph showing all the absorption spectra for the various iodide/triiodide samples.

Table E.5: The concentrations that were obtained from fitting data to the absorption spectra from figure E.3.

	$Fe(CN)_6^{3-}$ (M)	$Fe(CN)_6^{4-}$ (M)	I_3^- (M)	I^- (M)
Sample 1	0	0	0.558	0
Sample 2	0	0	0.90039	0
Sample 3	0	0	2.5047	0
Sample 4	0	0	1.00689	0

ICP-MS results

Table E.6: A table showing the results of the ICP-MS measurements for the ferro/ferricyanide samples. As can be seen the concentrations stay approximately equal for all the samples.

	Fe (g/L)	K (g/l)
Sample 1	31.4	87.2
Sample 2	31.1	88.1
Sample 3	32.5	91.5
Sample 4	31.4	88.7
Sample 5	31.7	88.8

Table E.7: A table showing the results of the ICP-MS measurements for the iodide/triiodide samples. As can be seen the iron concentration slightly increases over time. the potassium concentration drops between the fresh sample and all the other samples. Then it remains constant indicating an equilibrium.

	Fe (g/L)	K (g/l)
Sample 1	0.028	69.4
Sample 2	0.118	69.8
Sample 3	0.104	69.9
Sample 4	0.101	68.2
Sample 5	<1mg/l	75

XPS measurements of titanium electrode

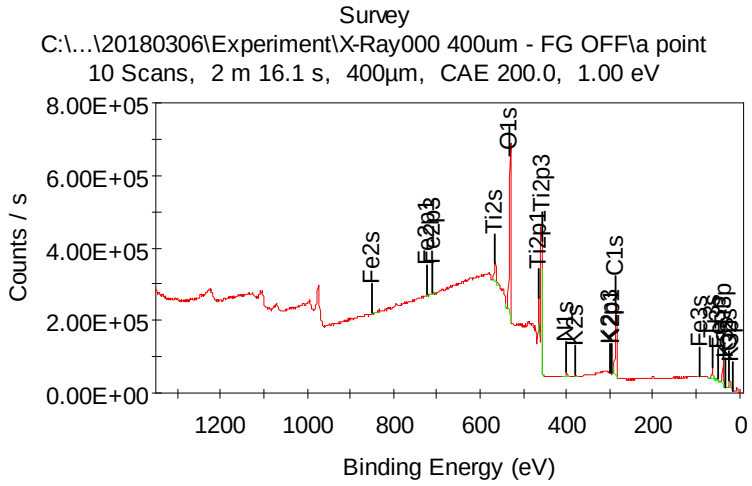
Survey
C:\...\20180306\Experiment\X-Ray000 400um - FG OFF\a point
10 Scans, 2 m 16.1 s, 400µm, CAE 200.0, 1.00 eV
Counts / s
8.00E+05
6.00E+05
4.00E+05
2.00E+05
0.00E+00
Fe2s
Ti2s
O1s
Ti2p3
Ti2p1
C1s
1200
1000
800
600
400
200
0
Binding Energy (eV)

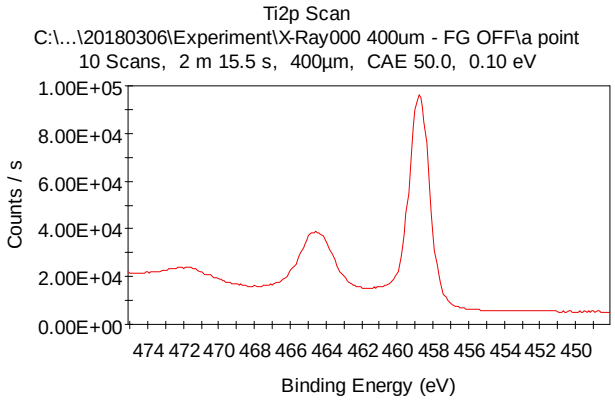
Ti2p Scan
C:\...\20180306\Experiment\X-Ray000 400um - FG OFF\a point
10 Scans, 2 m 15.5 s, 400µm, CAE 50.0, 0.10 eV
Counts / s
1.00E+05
8.00E+04
6.00E+04
4.00E+04
2.00E+04
0.00E+00
474 472 470 468 466 464 462 460 458 456 454 452 450
Binding Energy (eV)

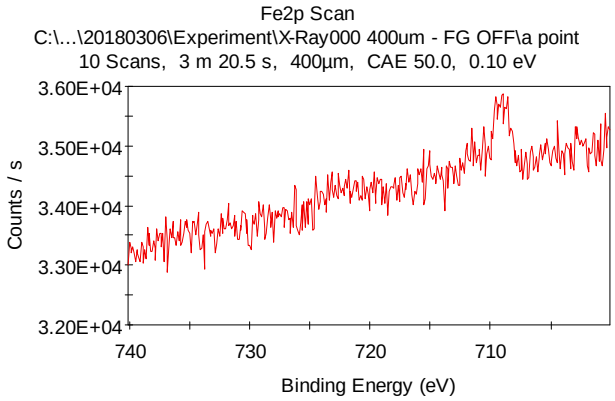
Fe2p Scan
C:\...\20180306\Experiment\X-Ray000 400um - FG OFF\a point
10 Scans, 3 m 20.5 s, 400µm, CAE 50.0, 0.10 eV
Counts / s
3.60E+04
3.50E+04
3.40E+04
3.30E+04
3.20E+04
740
730
720
710
Binding Energy (eV)

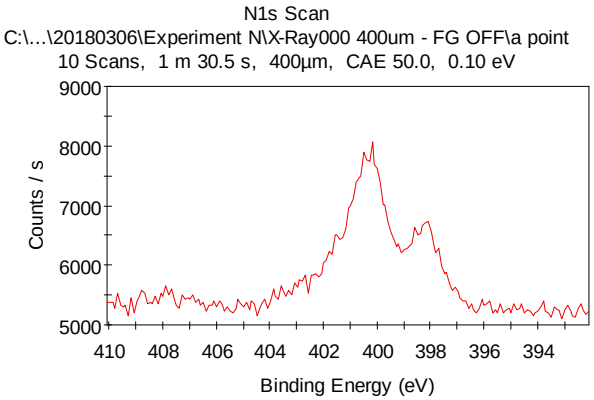

Elemental ID and Quantification

Name	Peak BE	FWHM eV	Area (P) CPS.eV	Atomic %	Q
O1s	530.45	2.14	1635351.58	29.02	1
C1s	285.17	2.92	643149.71	27.63	1
Ti3s	62.20	3.57	126361.23	14.29	1
Ti3p	37.13	3.15	239822.95	11.65	1
Ti2s	565.00	5.03	292021.83	6.24	1
O2s	22.39	0.80	17141.60	5.42	1
Ti2p1	464.30	1.73	159543.98	3.77	1
N1s	399.91	3.83	53914.52	1.49	1
Fe3p	50.12	2.74	14494.21	0.36	1
K2s	378.24	1.63	2554.56	0.06	1
Fe2p3	709.70	1.21	4771.95	0.03	1
Fe3s	93.12	0.31	362.77	0.03	1
Fe2s	849.39	0.00	407.20	0.01	1
Fe2p1	723.08	0.13	-17.43	0.00	1
Ti2p3	458.08	0.00	-13092.25	0.00	1
K2p1	295.95	0.00	-4100.30	0.00	1
K2p3	300.08	0.00	-77475.73	0.00	1
K3s	31.08	0.00	-33962.55	0.00	1
K3p	15.08	0.00	-5535.77	0.00	1

F

Calculations

Heat exchanger sizing

Using the following correlations and equations the heat exchanger was sized. It was done iteratively until the point was reached where the cold inlet temperature was equal to 20°C. Due to a lack of data on the actual solutions, the properties of water were assumed for most parameters. Table F.1 shows the various parameters that were used to perform the various calculations.

The equation to describe the temperature change is as follows:

$$T_{x+1} = T_{0,x} - e^{\frac{4Ux}{\rho c_p v D}} * (T_{0,x} - T_x) \tag{F.1}$$

where,

$$T_{0,x+1} = T_{0,x} - (T_x - T_{x+1}) \tag{F.2}$$

and

$$U = \frac{1}{h_i} + \frac{d}{\lambda_w} + \frac{1}{h_e} \tag{F.3}$$

To calculate the various components of U, the Graetz and Nusselt numbers were required which were defined as:

$$< Nu >= 1.62 * Gz^{-1/3} \quad \text{for} \quad Gz < 0.1 \quad \text{otherwise} \quad Nu = 3.66 \tag{F.4}$$

$$Gz = \frac{ax}{D^2 v} \tag{F.5}$$

which gives,

$$h_{i,e} = \frac{D}{Nu\lambda_{i,e}} \tag{F.6}$$

Once the x was known the total heat exchange surface area could be calculated using:

$$A = \pi * D * x \tag{F.7}$$

Table F.1: Table containing the various parameters that were used to do the calculations for the sizing of the heat exchanger.

Parameters

Definition	**Unit**	**Value**	**Definition**	**Unit**	**Value**
Density (ρ)	kg/m^3	1080	Step distance (x)	m	0.1
Heat capacity (c_p)	J/gK	4.2	Thermal conductivity water ($\lambda_{i,e}$)	W/mK	0.6
Diameter (D)	m	0.008	Thermal conductivity glass (λ_w)	W/mK	1.11
Thickness (d)	m	0.001	Thermal diffusivity (a)	m^2/s	$1.44 * 10^{-7}$
Fluid velocity (v)	m/s	0.02			

Bibliography

[1] U.S. Energy Information Administration, "Average tested heat rates." https://www.eia.gov/electricity/annual/html/epa_08_02.html, 2018. [Online; accessed 9-April-2018].

[2] Ener G Rotors, "Waste heat." http://www.ener-g-rotors.com/waste-heat/, 2018. [Online; accessed 9-April-2018].

[3] Interreg Central Europe, "Low-grade waste heat utilization in the European Union." http://www.interreg-central.eu/Content.Node/CE-HEAT/Low-grade-waste-heat-utilization-in-the-European-Union.html, 2017. [Online; accessed 9-April-2018].

[4] BCS Incorporated, "Waste Heat Recovery: Technology and Opportunities in U.S. Industry," tech. rep., U.S. Department of Energy, March 2008.

[5] D. B. Gingerich and M. S. Mauter, "Quantity, quality, and availability of waste heat from united states thermal power generation," *Environ. Sci. Technol.*, vol. 49, pp. 8297–8306, July 2015.

[6] U.S. Energy Information Administration, "U.S. electricity generation." https://www.eia.gov/tools/faqs/faq.php?id=427&t=3, 2018. [Online; accessed 9-April-2018].

[7] Alphabet Energy, "Waste Heat to Power Eliminates Emissions." https://www.alphabetenergy.com/waste-heat-to-power-eliminates-emissions/, 2016. [Online; accessed 9-April-2018].

[8] U. Drescher and D. Brüggemann, "Fluid selection for the organic rankine cycle (orc) in biomass power and heat plants," *Applied Thermal Engineering*, vol. 27, pp. 223–228, Jan. 2007.

[9] Bine Informationsdienst, "Transforming waste heat into electricity." http://www.bine.info/fileadmin/content/Publikationen/Englische_Infos/ProjektInfo_1311_engl_internetx.pdf, 2011. [Online; accessed 10-April-2018].

[10] D. M. van de Bor, C. A. Infante Ferreira, and A. A. Kiss, "Low grade waste heat recovery using heat pumps and power cycles," *Energy*, vol. 89, pp. 864–873, Sept. 2015.

[11] Final Year Projects, "Design and implementation of thermoelectric generator." http://myprojectscope.blogspot.com/2014/01/design-and-implementation-of.html, 2018. [Online; accessed 25-June-2018].

[12] T. Seebeck, "Magnetische polarisation der metalle und erze durch temperatur-differenz," *Abh. Akad. Wiss. Berlin*, p. 289–346, 1822.

[13] X. F. Zheng, C. X. Liu, Y. Y. Yan, and Q. Wang, "A review of thermoelectrics research - recent developments and potentials for sustainable and renewable energy applications," *Renewable and Sustainable Energy Reviews*, vol. 32, pp. 486–503, Apr. 2014.

[14] R. C. O'Brien, R. M. Ambrosi, N. P. Bannister, S. D. Howe, and H. V. Atkinson, "Safe radioisotope thermoelectric generators and heat sources for space applications," *Journal of Nuclear Materials*, vol. 377, pp. 506–521, July 2008.

[15] Y. Xie, S.-j. Wu, and C.-j. Yang, "Generation of electricity from deep-sea hydrothermal vents with a thermoelectric converter," *Applied Energy*, vol. 164, pp. 620–627, Feb. 2016.

[16] TEGPRO, "Thermoelectric generator products." http://www.tegpro.com/thermoelectric-generator-products, 2018. [Online; accessed 9-April-2018].

[17] Thermoelectric Generator, "Thermoelectric generator products." https://thermoelectric-generator.com, 2018. [Online; accessed 9-April-2018].

[18] M. F. Dupont, D. R. MacFarlane, and J. M. Pringle, "Thermo-electrochemical cells for waste heat harvesting-progress and perspectives," *Chemical Communications*, 2017.

[19] T. Kim, J. S. Lee, G. Lee, H. Yoon, J. Yoon, T. J. Kang, and Y. H. Kim, "High thermopower of ferri/ferrocyanide redox couple in organic-water solutions," *Nano Energy*, vol. 31, pp. 160–167, 2017.

[20] H. Im, T. Kim, H. Song, J. Choi, J. S. Park, R. Ovalle-Robles, H. D. Yang, K. D. Kihm, R. H. Baughman, and H. H. Lee, "High-efficiency electrochemical thermal energy harvester using carbon nanotube aerogel sheet electrodes," *Nature communications*, vol. 7, p. 10600, 2016.

[21] T. J. Kang, S. Fang, M. E. Kozlov, C. S. Haines, N. Li, Y. H. Kim, Y. Chen, and R. H. Baughman, "Electrical power from nanotube and graphene electrochemical thermal energy harvesters," *Advanced Functional Materials*, vol. 22, no. 3, pp. 477–489, 2012.

[22] J. M. Nugent, K. S. V. Santhanam, A. Rubio, and P. M. Ajayan, "Fast electron transfer kinetics on multiwalled carbon nanotube microbundle electrodes," *Nano letters*, vol. 1, no. 2, pp. 87–91, 2001.

[23] M. S. Romano, J. M. Razal, D. Antiohos, G. Wallace, and J. Chen, "Nano-carbon electrodes for thermal energy harvesting," *Journal of nanoscience and nanotechnology*, vol. 15, no. 1, pp. 1–14, 2015.

[24] S. Uhl, E. Laux, T. Journot, L. Jeandupeux, J. Charmet, and H. Keppner, "Development of flexible micro-thermo-electrochemical generators based on ionic liquids," *Journal of electronic materials*, vol. 43, no. 10, p. 3758, 2014.

[25] P. F. Salazar, S. Kumar, and B. A. Cola, "Nitrogen-and boron-doped carbon nanotube electrodes in a thermo-electrochemical cell," *Journal of The Electrochemical Society*, vol. 159, no. 5, pp. B483–B488, 2012.

[26] T. J. Abraham, D. R. MacFarlane, and J. M. Pringle, "Seebeck coefficients in ionic liquids -prospects for thermo-electrochemical cells," *Chem. Commun.*, vol. 47, no. 22, pp. 6260–6262, 2011.

[27] T. J. Abraham, D. R. MacFarlane, R. H. Baughman, L. Jin, N. Li, and J. M. Pringle, "Towards ionic liquid-based thermoelectrochemical cells for the harvesting of thermal energy," *Electrochimica acta*, vol. 113, pp. 87–93, Dec. 2013.

[28] Y. Ito and T. Nohira, "Non-conventional electrolytes for electrochemical applications," *Electrochimica Acta*, vol. 45, no. 15, pp. 2611–2622, 2000.

[29] M. Bonetti, S. Nakamae, M. Roger, and P. Guenoun, "Huge seebeck coefficients in nonaqueous electrolytes," *The Journal of chemical physics*, vol. 134, no. 11, p. 114513, 2011.

[30] H. Zhou, T. Yamada, and N. Kimizuka, "Supramolecular thermo-electrochemical cells: Enhanced thermo-electric performance by host-guest complexation and salt-induced crystallization," *Journal of the American Chemical Society*, vol. 138, no. 33, pp. 10502–10507, 2016.

[31] A. H. Kazim, A. S. Booeshaghi, S. T. Stephens, and B. A. Cola, "Thermo-electrochemical generator: Energy harvesting & thermoregulation for liquid cooling applications," *Sustainable Energy & Fuels*, 2017.

[32] S. W. Hasan, S. M. Said, M. F. M. Sabri, A. S. A. Bakar, N. A. Hashim, M. M. I. M. Hasnan, J. M. Pringle, and D. R. MacFarlane, "High thermal gradient in thermo-electrochemical cells by insertion of a poly (vinylidene fluoride) membrane," *Scientific reports*, vol. 6, p. 29328, 2016.

[33] J. Bleeker, "Design of a low-grade heat to power conversion system, using flow batteries," master thesis, TU Delft, 2017.

[34] T. I. Quickenden and C. F. Vernon, "Thermogalvanic conversion of heat to electricity," *Solar Energy*, vol. 36, pp. 63–72, Jan. 1986.

[35] R. H. Hammond and W. M. Risen, "An electrochemical heat engine for direct solar energy conversion," *Solar Energy*, vol. 23, no. 5, pp. 443–449, 1979.

[36] M. Al Maimani, J. J. Black, and L. Aldous, "Achieving pseudo-'n-type p-type'in-series and parallel liquid thermoelectrics using all-iron thermoelectrochemical cells with opposite seebeck coefficients," *Electrochemistry Communications*, vol. 72, pp. 181–185, 2016.

[37] L. Zhang, T. Kim, N. Li, T. J. Kang, J. Chen, J. M. Pringle, M. Zhang, A. H. Kazim, S. Fang, and C. Haines, "High power density electrochemical thermocells for inexpensively harvesting low-grade thermal energy," *Advanced Materials*, vol. 29, no. 12, 2017.

[38] W. Case, "Apparatus for converting heat energy into electrical energy." U.S. Patent 374173A, Dec 1886.

[39] S. W. Lee, Y. Yang, H.-W. Lee, H. Ghasemi, D. Kraemer, G. Chen, and Y. Cui, "An electrochemical system for efficiently harvesting low-grade heat energy," *Nature Communications*, 2014.

[40] A. Z. Weber, M. M. Mench, J. P. Meyers, P. N. Ross, J. T. Gostick, and Q. Liu, "Redox flow batteries: a review," *Journal of Applied Electrochemistry*, vol. 41, no. 10, p. 1137, 2011.

[41] M. Ulaganathan, V. Aravindan, Q. Yan, S. Madhavi, M. Skyllas-Kazacos, and T. M. Lim, "Recent advancements in all-vanadium redox flow batteries," *Advanced Materials Interfaces*, vol. 3, no. 1, 2016.

[42] Australian Vanadium, "All-vanadium redox flow battery." `http://australianvanadium.com.au/vanadium-batteries/`, 2018. [Online; accessed 11-January-2018].

[43] C. Blanc and A. Rufer, "Understanding the vanadium redox flow batteries," in *Paths to Sustainable Energy*, InTech, 2010.

[44] Selemion, "Selemion ion exchange membranes." `https://www.amp-ionex.com/products/selemion/pdf/selemion.pdf`, 2013. [Online; accessed 10-April-2018].

[45] D. A. Vermaas and W. A. Smith, "Synergistic electrochemical co2 reduction and water oxidation with a bipolar membrane," *ACS Energy Lett.*, vol. 1, pp. 1143–1148, Dec. 2016.

[46] M. Mäntynen, "Temperature correction coefficients of electrical conductivity and of density measurements for saline groundwater." `http://www.posiva.fi/files/2094/POSIVA-2001-15_Working-report_web.pdf`, 2001. [Online; accessed 23-April-2018].

[47] Emerson Process Management, "Conductance Data For Commonly Used Chemicals." `http://www2.emersonprocess.com/siteadmincenter/pm%20Rosemount%20Analytical%20Documents/LIQ_MAN_6039_Conductance_Data_Commonly_Used_Chemicals.pdf`, 2010. [Online; accessed 23-April-2018].

[48] A. Tang, J. Bao, and M. Skyllas-Kazacos, "Studies on pressure losses and flow rate optimization in vanadium redox flow battery," *Journal of power sources*, vol. 248, pp. 154–162, 2014.

[49] A. Da Costa, A. Fane, and D. Wiley, "Spacer characterization and pressure drop modelling in spacer-filled channels for ultrafiltration," *Journal of membrane science*, vol. 87, no. 1-2, pp. 79–98, 1994.

[50] I. Ruff, V. J. Friedrich, and K. Csillag, "Transfer diffusion. iii. kinetics and mechanism of the triiodide-iodide exchange reaction," *The Journal of Physical Chemistry*, vol. 76, no. 2, pp. 162–165, 1972.

[51] Engineering Toolbox, "Thermal Expansion coefficiencts." `https://www.engineeringtoolbox.com/linear-expansion-coefficients-d_95.html`, 2018. [Online; accessed 13-June-2018].

[52] P. Alotto, M. Guarnieri, and F. Moro, "Redox flow batteries for the storage of renewable energy: A review," *Renewable and Sustainable Energy Reviews*, vol. 29, pp. 325–335, Jan. 2014.

[53] A. Gunawan, C.-H. Lin, D. A. Buttry, V. Mujica, R. A. Taylor, R. S. Prasher, and P. E. Phelan, "Liquid thermoelectrics: review of recent and limited new data of thermogalvanic cell experiments," *Nanoscale and Microscale Thermophysical Engineering*, vol. 17, no. 4, pp. 304–323, 2013.

[54] C. Gao, S. W. Lee, and Y. Yang, "Thermally regenerative electrochemical cycle for low-grade heat harvesting," *ACS Energy Letters*, vol. 2, no. 10, pp. 2326–2334, 2017.

[55] Tweakers, "Xperia XZ specifications." https://tweakers.net/pricewatch/581117/sony-xperia-xz-zwart/specificaties/, 2018. [Online; accessed 12-June-2018].

[56] A. Szánto D., S. Cleghorn, C. Ponce-de-León, and C. Walsh F., "The limiting current for reduction of ferricyanide ion at nickel: The importance of experimental conditions," *AIChE J.*, vol. 54, pp. 802–810, Mar. 2008.

[57] S. Kireev and S. Shnyrev, "Study of molecular iodine, iodate ions, iodide ions, and triiodide ions solutions absorption in the uv and visible light spectral bands," *Laser Physics*, vol. 25, no. 7, p. 075602, 2015.

[58] I. M. Kolthoff and E. A. Pearson, "Stability of potassium ferrocyanide solutions," *Industrial & Engineering Chemistry Analytical Edition*, vol. 3, no. 4, pp. 381–382, 1931.